Draft version October 6, 2025
Typeset using LaTeX **twocolumn** style in AASTeX7.0.1

A $z \simeq 0.4$ Little Red Dot analog: An Extended Starburst with an Overmassive Black hole

Xiaoyang Chen [1,2] Kohei Ichikawa [1] Masayuki Akiyama [3] Kohei Inayoshi [4] Akio K. Inoue [2,5] Masafusa Onoue [6,7] Yoshiki Toba [8,9] Jorge Zavala [10] Tom Bakx [11] Toshihiro Kawaguchi [12] Kianhong Lee [13,3,14] Naoki Matsumoto [3] and Bovornpratch Vijarnwannaluk [15,3]

[1] *Frontier Research Institute for Interdisciplinary Sciences, Tohoku University, Sendai 980-8578, Japan*
[2] *Waseda Research Institute for Science and Engineering, Waseda University, 1-6-1 Nishi-Waseda, Shinjuku-ku Tokyo 169-8050, Japan*
[3] *Astronomical Institute, Tohoku University, 6-3 Aramaki, Aoba-ku, Sendai, Miyagi 980-8578, Japan*
[4] *Kavli Institute for Astronomy and Astrophysics, Peking University, 5 Yiheyuan Road, Haidian District, Beijing 100871, P. R. China*
[5] *Faculty of Science and Engineering, Waseda University, 1-6-1 Nishi-Waseda, Shinjuku-ku Tokyo 169-8050, Japan*
[6] *Waseda Institute for Advanced Study, Waseda University, 1-21-1, Nishi-Waseda, Shinjuku, Tokyo 169-0051, Japan*
[7] *Kavli Institute for the Physics and Mathematics of the Universe, UTIAS, Tokyo Institutes for Advanced Study, University of Tokyo, Chiba, 277-8583, Japan*
[8] *Department of Physical Sciences, Ritsumeikan University, 1-1-1 Noji-higashi, Kusatsu, Shiga 525-8577, Japan*
[9] *Research Center for Space and Cosmic Evolution, Ehime University, 2-5 Bunkyo-cho, Matsuyama, Ehime 790-8577, Japan*
[10] *Department of Astronomy, University of Massachusetts, LGRT-B 619E, 710 North Pleasant Street, Amherst, MA 01003-9305, United States*
[11] *Department of Space, Earth, & Environment, Chalmers University of Technology, Chalmersplatsen 4, 412 96 Gothenburg, Sweden*
[12] *Graduate School of Science and Engineering, 3190 Gofuku, Toyama City, Toyama, 930-8555, Japan*
[13] *Department of Physics, Graduate School of Science, Nagoya University, Furo, Chikusa, Nagoya, Aichi 464-8602, Japan*
[14] *National Astronomical Observatory of Japan, 2-21-1 Osawa, Mitaka, Tokyo 181-8588, Japan*
[15] *Institute of Astronomy and Astrophysics, Academia Sinicam 11F of Astronomy-Mathematics Building, AS/NTU, No.1, Sec. 4, Roosevelt Rd, Taipei 106319, Taiwan, R.O.C.*

(Received; Revised; Accepted)

Submitted to ApJ

ABSTRACT

One of the most remarkable discoveries of JWST is a population of compact, red sources at $z > 4$, commonly referred to as Little Red Dots (LRDs). Spectroscopic identifications reported that most LRDs are active galactic nuclei (AGNs), which are preferentially found around $z \sim 6$ and could imply a key phase in the formation and growth of black holes (BHs) in the early universe. Photometric surveys at lower redshift have recently been carried out to trace their evolution across cosmic time, and a small number of LRDs have been spectroscopically identified at both Cosmic Noon and in the local universe. Here we report the discovery of one of the lowest-z analogs of LRDs, J204837.26-002437.2 (hereafter J2048) at $z = 0.4332$, using new Gemini-N/GMOS IFU observations combined with archival multi-band photometric SED data. The GMOS data reveal extended blue emission from starburst with a star formation rate of 400 $M_\odot\,\mathrm{yr}^{-1}$, together with an extended, highly fast ionized outflow. This is the first spectroscopic confirmation of extended host emission and outflow in an LRD-like galaxy, providing a unique laboratory for understanding the nature of their high-redshift counterparts. Moreover, J2048 would host an extremely overmassive BH with a BH–to–stellar mass ratio of $\simeq 0.6$, with the BH mass and host stellar mass estimated to be $10^{10.2}$ and $10^{10.4}\,M_\odot$, respectively. We discuss the origin and evolutionary fate of J2048, and the implications that such low-z analogs have for interpreting the properties of high-z LRDs.

Keywords: Active galactic nuclei (16), Ultraluminous infrared galaxies (1735), Supermassive black holes (1663), AGN host galaxies (2017)

1. INTRODUCTION

The advent of JWST has revealed a previously unknown population of compact, red sources at $z > 4$, commonly referred to Little Red Dots (LRDs; e.g., Matthee et al. 2024). These sources show a distinctive v-shaped spectral energy distribution (SED), characterized by a blue continuum in the rest-frame UV, a red continuum in the rest-frame optical bands, with a turnover near the Balmer break (Kocevski et al. 2023, 2025; Barro et al. 2024; Furtak et al. 2023; Greene et al. 2024; Setton et al. 2024; Wang et al. 2025). Spectroscopic follow-up has confirmed that over 60% of LRDs host broad Balmer emission lines, indicating the presence of active galactic nuclei (AGNs) with inferred black hole (BH) masses of $M_{\rm BH} \sim 10^{6-8}\ M_\odot$ (Maiolino et al. 2024; Greene et al. 2024; Hviding et al. 2025).

Despite their AGN signatures, most LRDs show weak near-IR (NIR) to mid-IR (MIR) emission and non-detections by ALMA bands, suggesting a lack of hot ($T \simeq 1000$ K) and warm ($T \simeq 300$ K) dust heated by the AGN torus (Leung et al. 2024; Pérez-González et al. 2024; Williams et al. 2024; Akins et al. 2024; Setton et al. 2025). It is discussed that a more extended dust distribution (> 10 pc) rather than typical AGN dusty region (e.g., Nenkova et al. 2008; Hönig 2019; Nikutta et al. 2021), along with new constraints on the dust content in LRDs from multiwavelength data (Casey et al. 2025), is required to explain the weak warm dust emission (Li et al. 2025b; Chen et al. 2025b). In addition, most LRDs lack X-ray detections with the exception of a few sources (Kocevski et al. 2025), indicating either significant obscuration or intrinsically weak corona emission, possibly related to a super-Eddington accretion phase (Ananna et al. 2024; Yue et al. 2024; Inayoshi et al. 2024).

The origin of the v-shape SED, or in other words, the blue excess in the rest-frame UV SED, is also under debate. Either a star-forming host galaxy or scattered AGN light is considered as possible explanations of the blue excess. Most LRDs are spatially unresolved with effective radii $\lesssim$ 100–300 pc (e.g., Akins et al. 2024; Kokorev et al. 2024). Several studies report extended emissions in JWST's imaging observations in rest-frame UV bands, which support the explanation with blue, young stars in their host galaxies (e.g., Rinaldi et al. 2024; Billand et al. 2025; Chen et al. 2025a; Zhuang et al. 2025). Billand et al. (2025) reports that the outskirt component could become more apparent with decreasing redshift due to the formation of host galaxies. However, due to the distance of the high-z LRDs, the extended features are very faint, which prevent us from a detailed view of the host properties of LRDs.

Corresponding author: Xiaoyang Chen
astro@xychen.me

It is suggested that a powerful outflow can have an important role in the evolution of LRDs, e.g., expelling gas from the inner AGN region, enlarge the galaxy size, enhance or suppress star formation (e.g. Billand et al. 2025; Wang et al. 2025). Outflow has been seen in several LRDs with JWST/NIRSpec observations with both emission lines (e.g., [OIII], Cooper et al. 2025; D'Eugenio et al. 2025) and absorptions (e.g., He I, Juodžbalis et al. 2024a; Wang et al. 2025), although the sample is very limited probably due to the faintness of outflow features.

Another key aspect of LRDs is their unexpectedly high number density at $z > 4$, reaching $\sim 10^{-4}$ Mpc^{-3}, at least two orders of magnitude higher (Kokorev et al. 2024; Kocevski et al. 2025) than the extrapolation of UV-selected quasars (Akiyama et al. 2018; Matsuoka et al. 2018, 2023; Kulkarni et al. 2019; Niida et al. 2020; He et al. 2024). The reason on different densities of LRDs and quasars is under debate, which is possibly due to selection bias of those surveys of LRDs and quasars, e.g., the current JWST survey area is not sufficient to find rare bright quasars. The different densities can be also explained by the different evolutionary phases of black holes through cosmic time (Inayoshi & Ichikawa 2024; Inayoshi 2025). Unlike quasars whose number density declines toward higher redshift, the LRD population appears to increase with redshift, suggesting that they may represent a distinct phase in black hole evolution, possibly corresponding to the earliest growth stage of supermassive BHs (SMBHs) with their BH masses roughly two orders of magnitude smaller than the typical ones in luminous quasars (Greene et al. 2024; He et al. 2024).

The current JWST surveys imply a sharp decline in the abundance of LRDs at $z < 4$ (e.g., Inayoshi & Ichikawa 2024). In order to explore evolution of LRDs through cosmic time, several recent efforts have sought to identify LRDs at lower-z ($z < 4$) using optical and NIR photometry, e.g., Kocevski et al. (2025, JWST imaging surveys), Euclid Collaboration et al. (2025, Euclid Quick Release 1), and Ma et al. (2025, UltraDeep fields of the Subaru/HSC SSP survey). These studies confirm the decline of LRDs's number density as redshift decreases, though the values of the number densities are still diverse probably due to contamination of other type objects in LRD identifications (e.g., Euclid Collaboration et al. 2025). A small number of LRDs have been identified with spectroscopic observations at Cosmic Noon ($z \sim$ 2–3; Noboriguchi et al. 2023; Juodžbalis et al. 2024a; Billand et al. 2025; Ma et al. 2025; Stepney et al. 2024; Rinaldi et al. 2025; Wang et al. 2025) and in the local universe (Lin et al. 2025). Utilizing observations with higher S/N and wider wavelength coverage, those lower-z LRDs can be used as a window to witness the properties of the LRDs at $z > 4$ by exhibiting more detailed properties.

In this paper, we present the discovery and spectroscopic confirmation of one of the lowest-z analog

of LRDs, J204837.26-002437.2 (hereafter J2048) at[16] $z = 0.4332$, by utilizing new Gemini-N/GMOS observations as well as archived multi-band photometric SED. J2048 exhibits features similar to those of the high-z LRDs, such as a v-shape SED in UV and optical bands as well as a compact, red continuum from a reddened AGN. The GMOS observation shows extended blue emission from young stars and extended, highly fast ionized outflow. This is the first time that the extended host emission and outflow is spectroscopically confirmed in a LRD-like galaxy, providing a unique laboratory to study the nature of those distant LRDs. We report the observation in Section 2 and analysis methods in Section 3. The results on AGN, host galaxy, and emission line properties are shown in Section 4. The comparison of observational properties (e.g., v-shape SED and red continuum) between J2048 and high-z ($z > 4$) LRDs is discussed in Section 5.1; the implications on high-z LRDs from the observations of J2048 is discussed in Section 5.2; the extremely overmassive SMBH is discussed in Section 5.3. Cosmological parameters $H_0 = 67.4\,\mathrm{km\,s^{-1}\,Mpc^{-1}}$ and $\Omega_\mathrm{M} = 0.315$ (Planck Collaboration et al. 2020) are adopted throughout the paper.

2. SAMPLE AND DATA

2.1. *Sample Selection*

J2048 is one of the ultra-luminous IR galaxies (ULIRGs) at intermediate redshifts ($0.1 < z < 1.0$), which were selected from the cross-matched all-sky survey catalogs of AKARI (far-IR) and Wide-field Infrared Survey Explorer (WISE, NIR and MIR) as well as the Sloan Digital Sky Survey (SDSS, optical) spectroscopic catalog (Chen et al. 2020). The parent sample is selected with the entire IR luminosity ($L_{1\text{-}1000\mu\mathrm{m}}$) higher than $10^{12}\,L_\odot$. Eight ULIRGs including J2048 exhibit highly fast ionized outflows ($> 1500\,\mathrm{km\,s^{-1}}$) in their blueshifted, broad [OIII] 5007Å line profiles. Integral field unit (IFU) follow-up observations with Gemini/GMOS and Subaru/FOCAS were conducted for the ULIRGs to understand the spatial extent and kinetic power of these extreme outflows. Compared to the spatially-unresolved and fiber-aperture-limited spectroscopic data of the SDSS legacy survey, the new IFU follow-ups provide spatially-resolved data for the entire galaxies and cover longer wavelength ranges up to 1.05 μm. A compact red continuum and a broad Hα line from the AGN Broad Line Region (BLR) are newly detected in the Gemini/GMOS observation of J2048, which are not shown in the SDSS archived spectrum due to its limited spectral coverage. We show the observational details in the next subsection.

[16] The systemic redshift is estimated with narrow Hα line. See Section 3.1 and 4.3 for details.

2.2. *Gemini-N/GMOS IFU observations*

J2048 was observed by Gemini-N/GMOS in 2022 July (ID: GN-2022A-Q-221, PI: Chen). The observation was conducted with a total of 2.5 hours on-source exposure in two nights in the 2-slit IFU mode of GMOS. The 2-slit IFU mode has a field of view (FoV) of $5'' \times 7''$ with a pixel scale of $0.2''$. The FoV and position angle of the observation are shown in Figure 1. The Point Spread Function (PSF) of the IFU data has a Full Width Half Maximum (FWHM) of $\sim 0.65''$ in i-band ($\sim$ 7500Å), which is estimated with stellar objects in the acquisition images of the observations. The grating R150 was utilized to achieve a wide wavelength coverage, i.e., from [OII] 3726Å line to [SII] 6731Å line (Figure 2), which provides a spectral resolution of R $\sim$ 1000 ($\sim 300\,\mathrm{km\,s^{-1}}$) around 7000Å. The wavelength accuracy estimated with night sky emission lines is $\sim 50\,\mathrm{km\,s^{-1}}$. The observation has a spectral pixel scale ($\Delta\lambda$) of 3.9Å.

The GMOS data is reduced with the Gemini IRAF package (Gemini Observatory & AURA 2016), e.g., to calibrate the wavelength, mask bad pixels, remove the scattered light, correct for the atmospheric dispersion, and subtract the night sky emissions. We follow the same reduction pipeline adopted in Chen et al. (2025c) and recommend readers to check the details in this paper.

2.3. *Archive observations*

We collect the multi-wavelength photometric observations of J2048 in archives of the following telescopes and instruments: SDSS (u' to z' bands), 2MASS (J, H, and K_s bands), WISE (3.4, 4.6, 12, and 22 μm), Spitzer IRAC (3.6, 4.5, 5.8, and 8 μm) and MIPS (24 μm). The photometric fluxes are shown in Figure 3. A simultaneous fitting for the new GMOS spectrum and the archived photometric data is performed with the method described in Section 3.2.

3. ANALYSIS METHOD

3.1. *Spectral fitting for the GMOS IFU spectra*

In order to determine the spatial extents of the host and AGN components, we perform per-pixel spectral fitting for the GMOS IFU data cube utilizing our fitting code[17] `S3Fit` (Chen 2025; Chen et al. 2025c). The stellar continuum is fit utilizing an old stellar population (OSP) with an exponentially decayed star formation history (SFH), and a young stellar population (YSP) with constant star formation rate (SFR). Both of OSP and YSP are built using the single stellar population (SSP) library of PopStar (Millán-Irigoyen et al. 2021) with the initial mass function (IMF) of Kroupa (2001). A power-law component ($f_\lambda \propto \lambda^{\alpha_\mathrm{PL}}$) is adopted to represent the radiation from the AGN accretion disk.

[17] https://github.com/xychcz/S3Fit

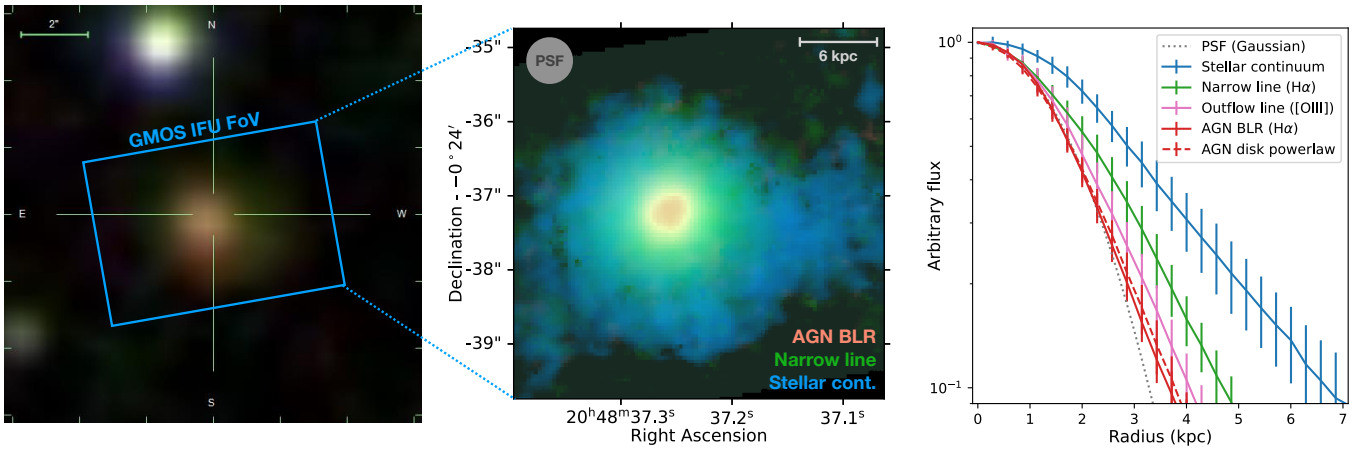

Figure 1. Left: SDSS *gri*-bands composite image of J2048. The field of view of the GMOS IFU observation is over-plotted as a blue rectangular. **Middle:** Composite image of J2048 from the best spectral fitting results of GMOS IFU data. The red, green, and blue colors denote the AGN BLR Hα line, narrow Hα line, and young stellar continuum (integrated in rest frame 3500–4000 Å), respectively. The grey circle shows the PSF FWHM of 0.65″. **Right:** Average radial profiles of young stellar continuum (blue; 3500–4000 Å), narrow Hα line (green), outflow [OIII] line (purple; the "outflow line 1" component in Figure 2), AGN BLR (red solid) and disk power-law component (red dashed). The profiles are arbitrarily normalized at the center. An approximate PSF using a Gaussian profile with FWHM of 0.65″ is shown in grey dotted line, which can reproduce the bulk of the unresolved AGN BLR and power-law components.

The GMOS spectra covers a wide emission line range from [OII] to [SII] (Figure 2). Two Gaussian profiles are used to fit each line, with a narrow profile (FWHM $<$ 750 km s^{-1}) for the emission from dynamically quiescent gas, and a broad profile (750 $<$ FWHM $<$ 2500 km s^{-1}) for the emission from outflowing gas. A secondary outflow profile with velocity shift (v_s) $<$ $-$1000 km s^{-1} is required to describe the blueshifted wings of [OIII] and Hα-[NII] complex. Furthermore, we use an additional broad profile (FWHM $>$ 5000 km s^{-1}) to model the gas emission in the AGN BLR. The BLR profile is only detected in Hα due to high dust extinction (see discussion in Section 4.1) and thus disabled for other Hydrogen Balmer lines.

We employ the following methods to reduce the degeneracy in the fitting. (1) A solar metallicity is adopted for stellar components, which is found as a typical value in local (U)LIRGs (e.g., Pérez-Torres et al. 2021). The extinction of stellar continuum ($A_{V,*}$) is adopted as $0.5A_{V,\rm NL}$, where $A_{V,\rm NL}$ is estimated from the Balmer decrement[18] of narrow lines with the extinction law of Calzetti et al. (2000); the factor 0.5 is an typical stellar-to-nebular extinction ratio in starburst galaxies (e.g., Calzetti 1997; Chen et al. 2025c). The effect of the assumed extinction ratio on estimation of properties (e.g., stellar mass) is discussed in Section 4.2. (2) The AGN power-law index ($\alpha_{\rm PL}$) is fixed to -1.7, which is a typical value in composite quasar templates (e.g., Francis et al. 1991; Vanden Berk et al. 2001; Selsing et al. 2016; Temple et al. 2021). The effect of the assumed index on estimation of properties (e.g., bolometric luminosity) is discussed in Section 4.1. The extinction of the power-law continuum ($A_{V,\rm PL}$) is a free fitting parameter following the extinction law of Calzetti et al. (2000). (3) For either narrow or outflow line profiles, we tie the kinematic parameters, i.e., v_s and FWHM, of each emission line (e.g., [OII] and Hα). In addition, the v_s of BLR Hα line is tied to v_s of the narrow line component, assuming that both of them reflect the systemic redshift. (4) The flux ratios of neighboring lines of the same ions are fixed to their theoretical values, e.g., [OIII] 4959,5007Å and [NII] 6548,6583Å(Storey & Zeippen 2000); or the values calculated with `PyNeb` (Luridiana et al. 2015), e.g., [OII] 3726,3729Å, with the electron density estimated from the [SII] 6716,6731Å doublets and an assumed electron temperature of 10^4 K. We recommend readers to check the document[19] of `S`^{3}`Fit` for details of the line setup.

Monte Carlo simulations are used to estimate the uncertainty of each fitting parameter. For each observed spectrum, we generate 100 mock spectra via adding random noise normalized by the measurement errors, and perform spectral fitting for the mock spectra. The stan-

[18] The adopted intrinsic Hα/Hβ ratio is 2.863, assuming Case B recombination with electron temperature of 10^4 K and electron density of 10^2 cm^{-3} (Hummer & Storey 1987). The adopted electron density is consistent to the value estimated from the narrow [SII] 6716,6731Å doublets of the integrated spectrum, $10^{2.1\pm0.1}$ cm^{-3}.

[19] https://github.com/xychcz/S3Fit/blob/main/manuals/basic_usage.md

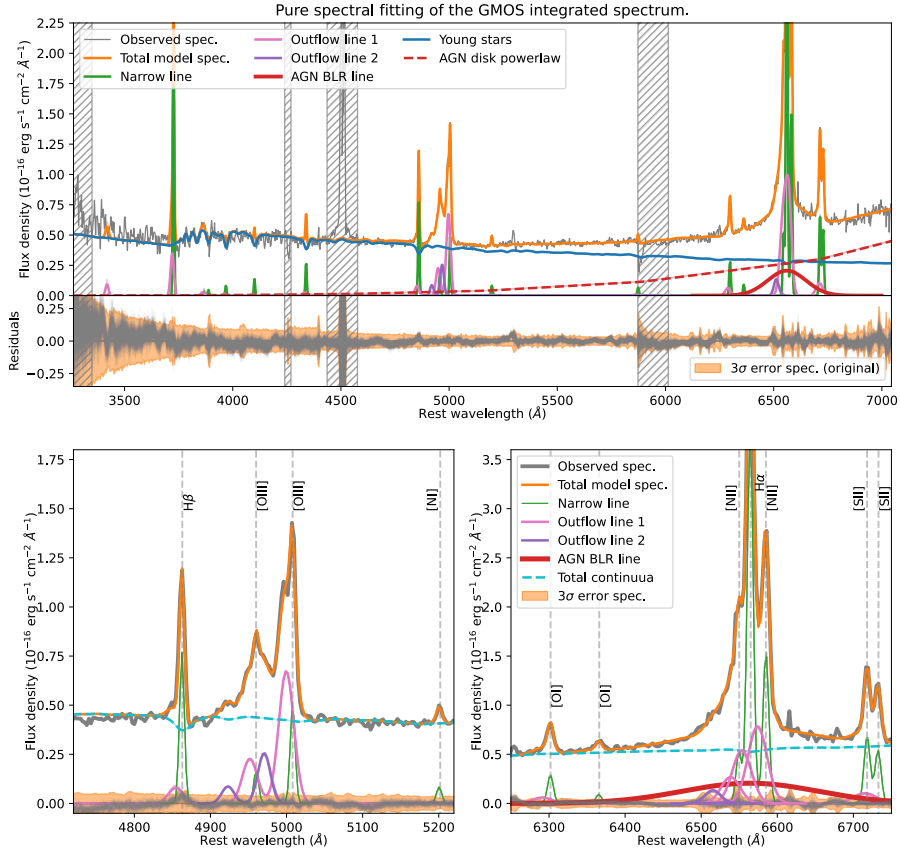

Figure 2. Best-fit results of the pure spectral fitting (Section 3.1) for the GMOS spectrum of the entire galaxy with fitting residuals (top and middle panels), as well as two zoomed-in regions around Hβ-[OIII] (bottom-left) and Hα-[NII] (bottom-right), respectively. The observed spectrum is shown in grey. The total model is shown in orange, with the young stellar continuum in blue and the AGN power-law component in red dashed lines. Emission lines include the narrow component (green), two broad blueshifted outflows (purple and violet), and the BLR Hα line (thick red). Grey hatched areas are excluded due to poor data quality. Note that in the top panel, the outflow profiles of the sum of Hα-[NII] complex are shown for the sake of illustration.

dard deviations of best-fit parameters of the simulated spectra are used as the uncertainties of best-fit parameters of observed spectra.

The map of AGN, stellar, and emission line components as well as the average radial profiles of them are shown in Figure 1. The best-fit results for the integrated spectrum of the entire galaxy (i.e., in the region shown in the middle panel of Figure 1) are shown in Figure 2. We discuss these results in details in Section 4.

3.2. *Simultaneous fitting for the GMOS integrated spectrum and multi-band photometric SED*

The fitting of the reddened AGN power-law component is sensitive to the spectrum at $\lambda > 6000$ Å (rest frame), which can be affected by the cutoff and moderate S/N of GMOS spectral observation at the long wavelength end. The fitting of the power-law model can in turn, affect other components such as the stellar continuum. In order to improve the fitting quality and to obtain better constraints on parameters (e.g., extinction of the AGN power-law), we employ a simultaneous fitting for the integrated GMOS spectrum and the archived multi-band photometric data from UV to MIR range.

The simultaneous fitting is performed with the `S`^{3}`Fit` in the joint spectrum+SED fitting mode. We keep using the same configurations of continuum and emission line models in Section 3.1 and add the SKIRTor AGN torus model (Stalevski et al. 2016) to extend the fitting to NIR-MIR range[20]. The AGN power-law continuum is declined at $\lambda > 5\mu$m with $\alpha_{\rm PL} = -4$, which corresponds to the Rayleigh-Jeans branch of the thermal emission from the outer region of the accretion disk (e.g., Schartmann et al. 2005; Feltre et al. 2012; Stalevski et al. 2016).

`S`^{3}`Fit` works by minimizing the reduced chi-square value:

$$\chi^2_\nu = \frac{1}{\Sigma_i w_i - n_{\rm par}} \Sigma_i \left[w_i \left(\frac{D_i - M_i}{E_{i,\rm mod}} \right)^2 \right], \qquad (1)$$

[20] We do not use the interstellar medium (ISM) dust model in the fitting since it only contributes to $< 10\%$ of fluxes in NIR-MIR range for J2048 (Chen et al. 2020). The best-fit ISM model of Chen et al. (2020) is shown in Figure 3 as a reference.

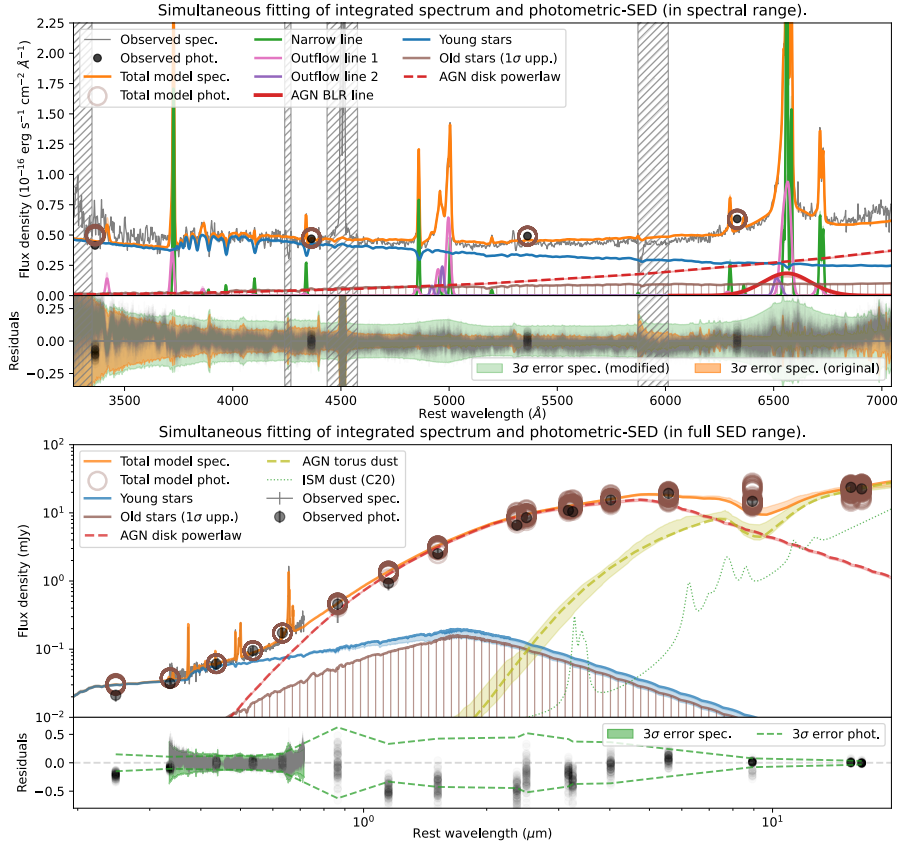

Figure 3. Best-fit results of the simultaneous spectrum+SED fitting (Section 3.2) for observations of the entire galaxy in the wavelength range of the spectrum (top) and all used SED data (lower-middle; rest-frame 0.2–20 μm) with their fitting residuals, respectively (upper-middle and bottom panels). Black dots and brown open circles denote the photometric data and the best-fit models, respectively. The legends of models are the same as those used in Figure 2. The AGN torus model is denoted in yellowgreen dashed curve. Shaded areas show the 25%–75% uncertainty ranges from Monte Carlo simulation for each component. The unconstrained old stellar population is shown as a 1σ upper limit (brown hatched; Section 4.2). The best-fit ISM dust model of J2048 from Chen et al. (2020) is shown in green dotted line as a reference. Note that all the residuals in the upper-middle and bottom panels are shown in unit of F_λ (10^{-16} erg s^{-1} cm^{-2} Å^{-1}) for the sake of illustration. The scatters reflect the fitting residuals of the original and mock data of the spectra (grey curves) and photometric points (black dots). Modified errors (to reflect the calibration errors) are shown in green shadow region and dashed lines.

where $n_{\rm par}$ is the number of used model parameters. D_i and M_i are the data and total model flux at each wavelength pixel and photometric band. w_i is the weight to balance the fitting of spectroscopic and photometric data. We adopt $w = R\Delta\lambda/\lambda$ for the spectrum, where R and $\Delta\lambda$ are the resolution and binning width of the spectrum; $w = 1$ is adopted for photometric data in each band. In order to account for calibration errors between different instruments, modified errors, $E_{i,\rm mod} = \sqrt{E^2_{i,\rm orig} + (10\%D_i)^2}$, are employed, where $E_{i,\rm orig}$ are the original measurement errors. The modified errors are also used to create mock data in the Monte Carlo estimation of fitting uncertainties as discussed in Section 3.1. In the calculation of $E_{i,\rm mod}$, the original spectral data D_i is convolved with a FWHM of 10^4 km s^{-1} to avoid involving artifacts into the mock spectral data around bright emission lines.

3.3. *Comparison and choice of results from the two fitting methods*

The best-fit results of the pure spectral fitting and the simultaneous spectrum+SED fitting for the spatially integrated data are shown in Figure 2 and 3, respectively. For the sake of a direct comparison between results of the two methods, we also extend the best-fit models of the pure spectral fitting to the full SED range in Figure A1. Due to the limited wavelength coverage of the GMOS spectrum, the AGN power-law model from the pure spectral fitting is not well constrained and cannot reproduce the observations in NIR range. Therefore, in the later analysis, we adopt the power-law properties (e.g., $A_{V,\rm PL}$ and luminosity) from the simultaneous spectrum+SED fitting. We also use the best-fit stellar properties (e.g., mass and SFR) from the simultaneous

spectrum+SED fitting, since it can be affected by the continuum decomposition with the power-law model.

On the other hand, the values of emission line properties (e.g., velocities and fluxes) estimated from the two methods only have slight differences (Table 1 and 2), except for the BLR Hα line, which is more sensitive to the fitting of the underlying continuum. The results of the simultaneous spectrum+SED fitting show larger uncertainties than those of the pure spectral fitting as the modified errors enlarge the fitting tolerance (e.g., Equation 1) and involve more scatters in the mock spectrum in Monte Carlo simulation, which are also reflected by the larger fitting residuals in Figure 3 (upper-middle panel). We adopt the results of emission lines from the pure spectral fitting throughout the paper since they are derived with a better subtraction of the underlying continuum, and their uncertainties directly reflect the measurement errors of the GMOS spectrum. The effect of result of BLR Hα line on the estimation of black hole mass is discussed in Section 4.1.

Table 1. Velocity shifts[a] (v_s) and FWHM[b] of each emission line component[c]

	v_s (km s^{-1})	FWHM (km s^{-1})
Narrow line	0.00 ± 0.91	357.41 ± 4.30
	0.08 ± 3.99	380.34 ± 15.24
Outflow line 1	-504.11 ± 17.92	1360.93 ± 27.13
	-496.30 ± 54.07	1350.00 ± 104.24
Outflow line 2	-2246.06 ± 27.90	1113.65 ± 61.13
	-2215.93 ± 98.57	1037.92 ± 156.12
AGN BLR line	0.00 ± 0.91	9517.29 ± 350.20
	0.08 ± 3.99	11853.13 ± 1810.78

[a]All of the v_s is relative to the systemic redshift $z = 0.4332$ estimated from the v_s of narrow line.

[b]All of the line widths are corrected for spectral resolution.

[c]For each component, the upper value is derived from the pure spectral fitting for the GMOS integrated spectrum (Section 3.1), which is adopted in default throughout the paper; the lower value is derived from the simultaneous fitting for the spectrum and the photometric SED (Section 3.2).

3.4. *Examination of AGN BLR and power-law components*

The AGN BLR Hα line and power-law continuum are related to the main finding of this work, i.e., a low-z LRD analog with an overmassive SMBH (Section 4.1 and 5). It is crucial to examine the detection of these components, i.e., if they are indeed required in the fitting, before detailed discussion of the results. We assess the significance of these components using the Akaike Information Criterion (AIC; Akaike 1974; Burnham & Anderson 2002) and the Bayesian Information Criterion (BIC; Schwarz 1978; Kass & Raftery 1995, following recommendations for astrophysical models (e.g., Takeuchi 2000; Liddle 2007). For a given dataset with noises following a Gaussian distribution, the criterion values can be calculated as $\Delta\mathrm{AIC} = 2\Delta n_{\mathrm{par}} + \Delta\chi^2$ and $\Delta\mathrm{BIC} = \Delta n_{\mathrm{par}}(\ln n_{\mathrm{data}}) + \Delta\chi^2$, where Δn_{par} is the difference of numbers of model parameters between two fitting configurations; n_{data} is the number of data points; $\Delta\chi^2$ is the difference of chi-square values between the two fitting results. A netagive criterion value, e.g., $\Delta\mathrm{AIC} = \mathrm{AIC}_{\mathrm{fit1}} - \mathrm{AIC}_{\mathrm{fit0}} < 0$, suggests the model configuration in fit1 is preferred.

We perform the fitting without BLR Hα or power-law components and calculate the ΔAIC and ΔBIC, respectively. The BLR Hα line is examined in rest-frame 6300–6800 Å (e.g., Figure 2, bottom-right panel). The pure spectral fitting results in $\Delta\mathrm{AIC} = \mathrm{AIC}_{\mathrm{w.BLR}} - \mathrm{AIC}_{\mathrm{w/oBLR}} = -1203$ and $\Delta\mathrm{BIC} = -1193$; the simultaneous spectrum+SED fitting results in $\Delta\mathrm{AIC} = -48$ and $\Delta\mathrm{BIC} = -38$, all of the tests support the requirement of BLR Hα line in the fitting. The power-law continuum is examined in the full SED range (e.g., Figure 3, lower-middle panel) and we get the criterion of ~ -1800 for both of ΔAIC and ΔBIC, which indicates that the power-law component is necessary to reflect the red bump in optical and NIR bands.

In addition to the AIC and BIC tests of the AGN power-law component, we also check if the red bump in optical and NIR SED can be explained by other models, e.g., a highly obscured old stellar continuum (Case 1) or a hidden starburst continuum (Case 2). The best-fit results of Case 1 and 2 are shown in Figure A2. In Case 1, the obscured old stellar continuum with $A_V = 5.7$ (brown dashed curve) can reproduce the red bump in SED (except for 1–3 μm). However, the derived stellar mass, $10^{13}\ M_\odot$, exceeds that of the most massive galaxies by one order of magnitude (e.g., Kormendy & Ho 2013). It is also unlikely that the bulk of the old stellar population is fully obscured by dust in optical bands as they mainly locate in diffuse interstellar medium (e.g., Charlot & Fall 2000). Therefore, it is unlikely that the observed red continuum is mainly contributed by obscured old stars. In Case 2, in addition to the young stellar population observed in UV and optical bands (blue solid curve in Figure A2), the best-fit result shows an additional hidden starburst component with $A_V = 7.2$ (cyan dotted curve). The hidden starburst corresponds to an unphysically high SFR of $10^5\ M_\odot\,\mathrm{yr}^{-1}$ in the recent ~ 10 Myr, suggesting that the possibility of a hidden starburst to explain the red bump can be ruled out.

To summarize, both of the AGN BLR Hα line and power-law continuum are required to explain the observed spectrum and SED; neither obscured old stars nor a hidden starburst could be a reasonable main contributor to the red bump in optical and NIR SED. Furthermore, we find that the power-law and BLR line com-

Table 2. Fluxes of each component of main emission lines[a]

	[OII] 3726Å	[OII] 3729Å	Hβ	[OIII] 5007Å	[OI] 6300Å	Hα	[NII] 6583Å	[SII] 6716Å	[SII] 6731Å
Narrow line	8.84 ± 0.28	11.93 ± 0.38	8.94 ± 0.23	6.01 ± 0.25	3.91 ± 0.18	54.05 ± 0.69	21.69 ± 0.55	9.75 ± 0.27	7.83 ± 0.20
	8.92 ± 0.46	12.04 ± 0.62	9.54 ± 0.53	6.16 ± 0.82	3.95 ± 0.51	56.83 ± 2.40	23.31 ± 2.07	10.35 ± 0.97	8.28 ± 0.80
Outflow line 1	4.06 ± 0.36	5.49 ± 0.49	2.72 ± 0.27	23.94 ± 0.42	2.72 ± 0.27	24.59 ± 1.05	35.90 ± 1.25	2.45 ± 0.38	3.22 ± 0.61
	4.46 ± 0.57	6.02 ± 0.77	2.04 ± 0.64	22.78 ± 1.14	1.37 ± 0.85	20.87 ± 3.97	35.14 ± 5.76	2.65 ± 1.14	1.89 ± 1.56
Outflow line 2	–	–	–	7.55 ± 0.37	–	4.99 ± 0.75	–[b]	–	–
	–	–	–	6.62 ± 1.03	–	4.58 ± 2.12	–	–	–
AGN BLR line	–	–	–	–	–	65.59 ± 1.87	–	–	–
	–	–	–	–	–	72.98 ± 7.34	–	–	–

[a]The fluxes are in unit of 10^{-16} erg s^{-1} cm^{-2}, which are the observed values and not corrected for the extinction. For each line component, the upper value is derived from the pure spectral fitting for the GMOS integrated spectrum (Section 3.1), which is adopted in default throughout the paper; the lower value is derived from the simultaneous fitting for the spectrum and the photometric SED (Section 3.2). The component with "-" is not used in the fitting due to their faintness.

[b]We enable the "Outflow line 2" component for [NII] doublets in the fitting, while they are not detected (Figure 2, bottom-right).

ponents show consistent morphologies and luminosities, which are discussed in details in Section 4.1.

4. RESULTS

4.1. *AGN properties*

The AGN is implied by the power-law continuum and the BLR Hα emission line. Both of the two components share the almost same, unresolved spatial profile (Figure 1, right panel), which can be described approximately using a Gaussian profile with FWHM of 0.65″.

The power-law continuum has a luminosity of $\lambda L_{5100} = 10^{12.81\pm0.11}\ L_\odot$ after extinction correction with $A_{V,\rm PL} = 6.28 \pm 0.27$, which are estimated from the simultaneous spectrum+SED fitting. The observed flux of the BLR Hα line is estimated as $10^{-14.18\pm0.01}$ erg s^{-1} cm^{-2} from the spectral fitting. Since the BLR Hβ line is too faint to be detected (e.g., Figure 2, bottom-left panel), we also adopt $A_{V,\rm PL} = 6.28$ for correction of BLR Hα line assuming that the BLR has the same amount of extinction as that of the AGN accretion disk (i.e., the power-law component). If we assume the peak of the BLR Hβ line with the 1σ noise level (Figure 2, bottom-left panel), the lower limit of $A_{V,\rm BLR}$ is estimated[21] to be 6.05, suggesting that the adopted $A_{V,\rm PL} = 6.28$ is a reasonable assumption. The intrinsic BLR Hα luminosity ($L_{\rm H\alpha,BLR}$) is estimated to be $10^{11.13\pm0.09}\ L_\odot$ (or $10^{44.72\pm0.09}$ erg s^{-1}). It is reported that the AGN optical and BLR Hα luminosities has a tight log-linear relation over a wide range of luminosities and redshifts (e.g., Greene & Ho 2005; Shen & Liu 2012; Jun et al. 2015). The ratio, $\log(L_{\rm H\alpha,BLR}/\lambda L_{5100}) = -1.7$, is 0.4 dex lower than the empirical relation of Jun et al. (2015), while the offset is within the distribution scatter of the sample to derive the relation (e.g., Figure 11 of Jun et al. 2015), indicating that our estimation of $L_{\rm H\alpha,BLR}$ and λL_{5100} are consistent.

In order to estimate the AGN bolometric luminosity ($L_{\rm AGN,bol}$), we employ an empirical optical bolometric correction, $L_{\rm AGN,bol}/\lambda L_{4400} = 5.1$ (Duras et al. 2020). The extinction-corrected λL_{4400} is estimated as $10^{12.85\pm0.11}\ L_\odot$ from the simultaneous spectrum+SED fitting. $L_{\rm AGN,bol}$ is then estimated to be $10^{13.56\pm0.11}\ L_\odot$, where the uncertainty corresponds to the scatters of λL_{4400} and $A_{V,\rm PL}$; the empirical bolometric correction can involve an additional spread of ~ 0.3 dex (Duras et al. 2020). The AGN torus IR luminosity ($L_{\rm AGN,torus}$) is estimated to be $10^{12.0\pm0.6}\ L_\odot$. The ratio, $\log(L_{\rm AGN,torus}/L_{\rm AGN,bol}) = -1.5$, is 0.4 dex lower than the typical value of AGNs at the high luminosity end ($\sim 10^{47}$ erg s^{-1}, e.g., Ichikawa et al. 2019). The ratio could imply that the covering factor of the dusty torus is relatively small, e.g., 0.2–0.3 (or a half-opening angle of 10°–20°), indicated by the energy balance of the absorbed emission of the central AGN and the reemitted radiation of torus in the SKIRTor model (Stalevski et al. 2016).

The black hole mass ($M_{\rm BH}$) can be estimated with the AGN optical luminosity (e.g., λL_{5100}) and the line width of the BLR Hα line following the empirical relation of Shen & Liu (2012):

$$\log\left(\frac{M_{\rm BH}}{M_\odot}\right) = 1.39 + 0.56\log\left(\frac{\lambda L_{5100}}{10^{44}\,{\rm erg\,s^{-1}}}\right) + 1.87\log\left(\frac{\rm FWHM_{H\alpha,BLR}}{\rm km\,s^{-1}}\right). \quad (2)$$

The FWHM of the BLR Hα line is estimated to be 9520 ± 350 km s^{-1} from the fitting of the integrated spectrum. The $M_{\rm BH}$ is then derived as $10^{10.17\pm0.07}\ M_\odot$. The shown uncertainties above corresponds to the scatters of λL_{5100} and $\rm FWHM_{H\alpha,BLR}$; the empirical calibration can involve an additional spread of ~ 0.1 dex.

Both of $L_{\rm AGN,bol}$ and $M_{\rm BH}$ are estimated with the power-law luminosity, which can be affected by the assumed power-law index ($\alpha_{\rm PL}$). $\alpha_{\rm PL}$ is fixed to -1.7 in the default fitting as it is a typical value for composite quasar templates (e.g., Temple et al. 2021). In order to understand the effect of assumed $\alpha_{\rm PL}$ on the estimation of $L_{\rm AGN,bol}$ and $M_{\rm BH}$, we test fitting with $\alpha_{\rm PL}$ in a range from -2.0 to -1.4. In the case with $\alpha_{\rm PL} = -2.0$, we get $A_{V,\rm PL} = 6.85$, $L_{\rm AGN,bol} = 10^{13.77}\ L_\odot$, and $M_{\rm BH} = 10^{10.28}\ M_\odot$; in the case with $\alpha_{\rm PL} = -1.4$, we get $A_{V,\rm PL} = 5.70$, $L_{\rm AGN,bol} = 10^{13.35}\ L_\odot$, and

[21] The adopted intrinsic Hα/Hβ ratio is 2.615, assuming Case B recombination with electron temperature of 10^4 K and electron density of 10^9 cm^{-3} (Hummer & Storey 1987).

$M_{\rm BH} = 10^{10.05}\ M_\odot$. Therefore, uncertainties of ±0.2 dex and ±0.1 dex can be involved in the estimation of $L_{\rm AGN,bol}$ and $M_{\rm BH}$, respectively, as the assumed $\alpha_{\rm PL}$ varies from −2.0 to −1.4.

$M_{\rm BH}$ can be also estimated using $L_{\rm H\alpha,BLR}$ and ${\rm FWHM_{H\alpha,BLR}}$. Utilizing the empirical calibrators of (Shen & Liu 2012, their Table 5), $M_{\rm BH}$ is derived to be $10^{9.87\pm0.05}\ M_\odot$ with $L_{\rm H\alpha,BLR}$ corrected using $A_{V,\rm PL} = 6.28$. If we adopt the lower limit of $A_{V,\rm BLR}$, 6.05, as discussed above, $M_{\rm BH}$ is estimated to be $10^{9.82}\ M_\odot$, which can be considered as an lower limit of $M_{\rm BH}$ estimated independently from the fitting of the power-law component.

As noted in Section 3.3, we use the best-fit results of emission lines from the pure spectral fitting throughout the paper. If we adopt ${\rm FWHM_{H\alpha,BLR}} = 11850 \pm 1810\ {\rm km\,s^{-1}}$ (Table 1) estimated from the simultaneous spectrum+SED fitting, the $M_{\rm BH}$ is estimated to be $10^{10.35\pm0.14}\ M_\odot$ with the default assumed $\alpha_{\rm PL} = -1.7$. We consider this value as an upper limit of $M_{\rm BH}$.

In the later discussion, we adopt fiducial values, $L_{\rm AGN,bol} = 10^{13.6\pm0.4}\ L_\odot$ and $M_{\rm BH} = 10^{10.2\pm0.2}\ M_\odot$, which are estimated utilizing the best-fit λL_{4400}, λL_{5100}, and ${\rm FWHM_{H\alpha,BLR}}$ with an assumed $\alpha_{\rm PL}$ of −1.7; the uncertainties in those values account for the uncertainties in the fitting results, the choice of assumed $\alpha_{\rm PL}$, and the scatters in the empirical calibrations (Shen & Liu 2012; Jun et al. 2015). Combining the estimated $L_{\rm AGN,bol}$ and $M_{\rm BH}$, the Eddington ratio of the AGN ($\lambda_{\rm Edd}$) is estimated to be 0.09 ± 0.01, suggesting the SMBH of J2048 is still growing via rapid accretion. The value is close to typical $\lambda_{\rm Edd}$ of high-z LRDs, 0.1–0.4 (e.g., Greene et al. 2024; Kokorev et al. 2023).

4.2. *Host galaxy properties*

Since the AGN power-law continuum emitting from the accretion disk is highly obscured in UV and optical bands, the spectrum of J2048 at rest-frame $\lambda < 6000$ Å is dominated by stellar continuum emitted by young stars even in the unresolved central region ($r < 1.8$ kpc; Figure A3, top panel). In the outskirt region ($r > 2$ kpc) where the AGN components are not detected, the full observed spectrum in dominated by stellar light (Figure A3, lower-middle panel). After correction for PSF using a Gaussian profile with FWHM of 0.65″, the average effective radius (i.e., the radius enclosing half of the entire flux) is estimated to be 3 kpc. The stellar disk is elongated to an effective radius of 7 kpc towards the west, showing a spiral arm-like structure in the direction (Figure 1, middle panel).

The best-fit results of the simultaneous spectrum+SED fitting suggest a total mass ($M_{\rm YSP}$) of $10^{9.9\pm0.1}\ M_\odot$ for the young stellar population, which was formed in the recent ∼ 20 Myr and corresponds to a mean SFR of $400 \pm 60\ M_\odot\,{\rm yr^{-1}}$ assuming a SFH with constant SFR. As noted in Section 3, in order to reduce the degeneracy in the fitting, the extinction of stellar continuum ($A_{V,*}$) is adopted as $0.5A_{V,\rm NL}$, where $A_{V,\rm NL}$ is estimated from the Balmer decrement of narrow lines and the factor 0.5 is an empirical stellar-to-nebular extinction ratio in ULIRGs (e.g., Chen et al. 2025c). The estimation of $M_{\rm YSP}$ and SFR can be affected by the adopted extinction ratio. We test the fitting with the extinction ratio in a range of 0.1–0.7 with the corresponding $A_{V,*}$ varying from 0.2 to 1.5; the fitting quality is poor with an extinction ratio over 0.7. The derived $M_{\rm YSP}$ varies from $10^{9.3}$ to $10^{10.1}\ M_\odot$ with the SFR from 100 to 600 $M_\odot\,{\rm yr^{-1}}$ in the test fits, which suggest the uncertainty ranges related to the assumed extinction ratio. The SFR can be also estimated independently with the IR luminosity emitted from ISM dust heated by stellar light. Utilizing $L_{\rm IR,SF} = 10^{12.5}\ L_\odot$ (Chen et al. 2020) and the empirical function (Calzetti 2013) under the same conditions[22], the IR-based SFR is estimated to be 450 $M_\odot\,{\rm yr^{-1}}$, which is consistent with the optical-based SFR from the default fitting result with a factor of 1.1.

The mass of the old stellar population ($M_{\rm OSP}$) is required to obtain the total stellar mass of the galaxy[23]. Stellar radiation from old stars typically peaks at NIR range (e.g., 1–3 μm), however, the archived NIR observations of J2048 is dominated by the reddened AGN power-law component, making it hard to directly estimate the mass of the old population. In order to estimate the upper limit of $M_{\rm OSP}$, we assume an oldest population (i.e., with the highest mass-to-light ratio) that was formed at $z = 10$ with an exponential timescale of 100 Myr. The spectrum+SED fitting is repeated by scanning a series of $M_{\rm OSP}$ values. The 1σ upper limit on $M_{\rm OSP}$ (i.e., the one-sided 84.1% confidence interval) is derived to be $10^{11.0}\ M_\odot$, which is defined as the value for which the profile-likelihood increases by $\Delta\chi^2_\nu = 1.35$ (e.g., Bevington & Robinson 2003; Wall & Jenkins 2012) from the best-fit case that shows zero OSP component. The OSP SED corresponding to the 1σ upper limit is shown as brown hatched regions in Figure 3.

With the above analyses, the total stellar mass (M_*) is constrained in a range from $10^{9.9}\ M_\odot$ (best-fit $M_{\rm YSP}$) to $10^{11.0}\ M_\odot$ ($M_{\rm OSP}$ upper limit). In later discussion, we adopt a fiducial value of $M_* = 10^{10.4}\ M_\odot$, which is estimated utilizing the average mass fraction of YSP, 0.3 ± 0.2, of 149 ULIRGs at $0.1 < z < 1$ (Chen et al. 2020). The fiducial M_* value corresponds to a specific SFR of $10^{-7.7}\ {\rm yr^{-1}}$, suggesting a vigorous starburst phase.

[22] SFR (in $M_\odot\,{\rm yr^{-1}}$) can be estimated as $3.7 \times 10^{44}\ L_{\rm IR,SF}$ (in ${\rm erg\,s^{-1}}$) for a young stellar population formed in 10 Myr with an IMF of Kroupa (2001) and a stellar mass range of 0.1–100 $M_\odot$ (Calzetti 2013).

[23] Due to the moderate spectral resolution and S/N of stellar absorption features, in this paper we do not use the stellar dispersion to estimate the dynamical mass.

4.3. *Extended narrow emission lines*

J2048 has an spatially extended narrow emission line region. The map and mean radial profile of narrow Hα line is shown in Figure 1, which correspond to an effective radius of 2.5 kpc after correction for PSF blurring. The FWHM of the narrow line component is estimated to be 357 ± 4 km s^{-1} using the integrated spectrum after correction for the spectral resolution (Table 1). Table 3 lists the flux ratios of emission lines that are used to determine the ionization energy source. It is indicated that the extended narrow lines are ionized by stellar light of young stars with the BPT diagnostics (Baldwin et al. 1981; Kewley et al. 2001; Kauffmann et al. 2003). The corresponding instantaneous SFR estimated using the extinction-corrected fluxes of the narrow Hα or [OII] lines are 140 ± 10 or 100 ± 20 $M_\odot$ yr^{-1}, respectively, utilizing the empirical functions of Calzetti (2013) and Kennicutt et al. (2009).

Table 3. Flux ratios of narrow and outflow emission lines.

Ratio	Narrow line	Outflow line 1
log([OIII]/Hβ)	-0.17 ± 0.02	0.94 ± 0.04
log([NII]/Hα)	-0.40 ± 0.01	0.16 ± 0.02
log([OI]/Hα)	-1.14 ± 0.02	-0.96 ± 0.05
log([SII]/Hα)	-0.49 ± 0.01	-0.64 ± 0.05

4.4. *Fast and powerful ionized outflow*

J2048 possesses a fast ionized outflow, which is indicated by the blueshifted, broad wings in profiles of all emission lines in the integrated spectrum (Fig. 2). The outflow wings dominate the line profiles of [OIII] 4959,5007Å doublets with a flux fraction of 84%. The [OIII] outflow have two components, a primary wing ("outflow line 1" in Figure 2) with v_s of -500 ± 20 km s^{-1} and FWHM of 1360 ± 30 km s^{-1} (Table 1); a secondary wing ("outflow line 2") with v_s of -2250 ± 30 km s^{-1} and FWHM of 1110 ± 60 km s^{-1}; the line widths are corrected for spectral resolution. The primary [OIII] outflow is marginally extended out of the PSF scale (Figure 1, right panel), with a PSF-corrected effective radius of 1.4 kpc. The secondary wing traces a faster outflow component while the component is unresolved in this observation. The log([OIII]/Hβ) ratio of the primary wing is 0.94±0.04 (Table 3). The Hβ line of the secondary wing is not detected and we can derive a lower limit of log([OIII]/Hβ), ~ 1.2, by assuming the peak of the Hβ line with the 1σ noise level (Figure 2, bottom-left panel). Those high [OIII]/Hβ flux ratio and upper limit imply that the fast outflowing gas is ionized by AGN.

We follow the method adopted in Chen et al. (2025c) to estimate the mass-loss rate and kinetic power of the fast ionized outflow. The gas mass of the ionized outflow ($M_{\rm out}$) can be derived with the fluxes of outflow components of [OII] 3729Å and [OIII] 5007Å lines, with the assumptions that the ionized outflow has a solar oxygen abundance and the oxygen ions are mainly in the singly and doubly ionized phases. The extinction in the outflow, $A_{V,\rm out} = 3.9 \pm 0.3$, is estimated using the Balmer decrement of the outflow lines. The electron density, $10^{3.1\pm0.8}$ cm^{-3}, is estimated with the outflow component of the [SII] doublets. The Oxygen-based[24] $M_{\rm out}$ is then estimated to be $10^{8.0\pm0.8}$ $M_\odot$ using the Equation (2) in Chen et al. (2025c). The timescale of the outflow can be derived as $\Delta t_{\rm out} = r_{\rm out}/v_{\rm out} = 0.7$ Myr; here we adopt the effective radius, 1.4 kpc, as the outflow traveling distance. The outflow velocity is calculated as $v_{\rm out} = |v_{50}| + w_{80}/2 = 2070 \pm 40$ km s^{-1}, where v_{50} and w_{80} are the 50% velocity and the 80% width of the sum of outflow 1 and 2 components of [OIII] (Figure 2, bottom-left panel). The time-averaged mass-loss rate is estimated to be $\dot{M}_{\rm out} = M_{\rm out} v_{\rm out}/r_{\rm out} = 160$ $M_\odot$ yr^{-1}. The kinetic power (or the kinetic energy ejection rate) is estimated to be $\dot{E}_{\rm k,out} = \dot{M}_{\rm out} v_{\rm out}^2/2 = 10^{44.3}$ erg s^{-1}.

The high velocity and kinetic power as well as the AGN-type ionization of the fast ionized outflow suggest that it is driven by AGN activity. The coupling factor of kinetic power, $\dot{E}_{\rm k,out}/L_{\rm AGN,bol} = 0.2\%$, is consistent with the values of luminous AGNs (e.g., Fiore et al. 2017). The high mass-loss and kinetic ejection rates indicate that the powerful outflow could have an important role in the galaxy evolution, e.g., by redistributing the fueling gas in the central and outskirt regions.

5. SUMMARY AND DISCUSSION

In this paper, we report a new discovery of an analog of LRDs at $z = 0.4$, J2048, utilizing the new GMOS optical IFU spectroscopic data and the archived multi-band photometric SED. J2048 has a v-shape SED in UV and optical bands as those appear in JWST-discovered LRDs at $z > 4$. The blue-excess is spatially extended and emitted from a starburst with SFR of 400 $M_\odot$ yr^{-1}. A compact red continuum in NIR and the BLR Hα line indicate an obscured AGN with $A_{V,\rm PL} = 6.3$, which corresponds to a bolometric luminosity of $10^{13.6}$ erg s^{-1}. The black hole mass is estimated to be $10^{10.2}$ $M_\odot$. J2048 also exhibits an extended, star formation ionized narrow line region and a concentrated, highly fast ionized outflow driven by the AGN, which suggest strong interaction between the AGN and the host galaxy.

We discuss the observational similarities of J2048 and high-z LRDs in Section 5.1. The implications on high-z LRDs from the observations of J2048 are discussed in Section 5.2 and the overmassive SMBH in Section 5.3.

[24] The $M_{\rm out}$ estimated from the flux of Hα outflow profile is $10^{8.1\pm0.8}$ $M_\odot$, which is consistent to the Oxygen-based result.

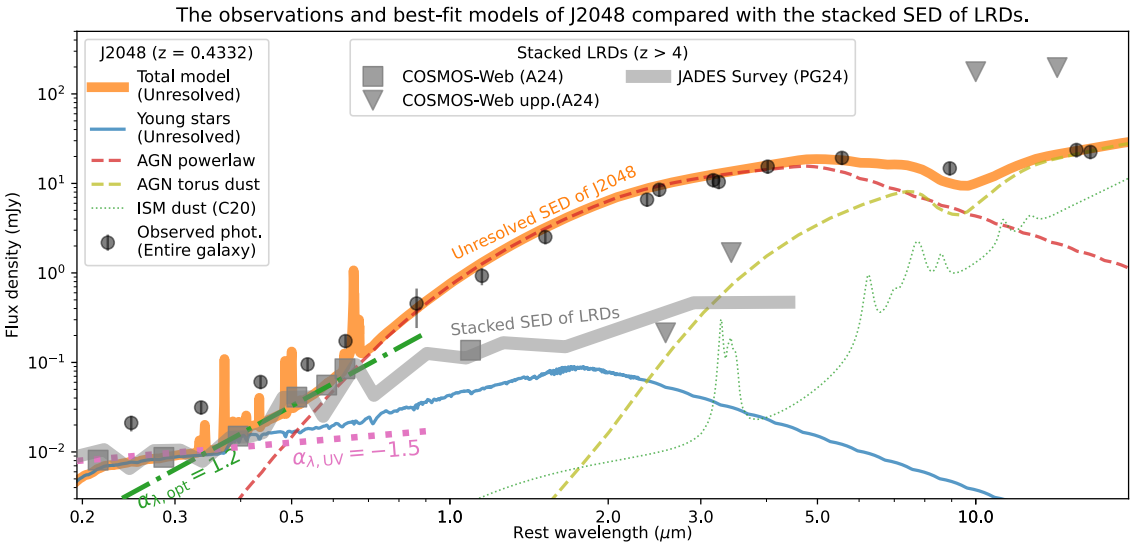

Figure 4. Best-fit models of the simultaneous spectrum+SED fitting for J2048 in the unresolved ($r < 2$ kpc) region of J2048. The unresolved SED (orange thick line) is obtained by subtracting the best-fit models of the extended outskirt region (Figure 5 and A3) from the best-fit SED of the entire galaxy (Figure 3). The best-fit power-law models for the unresolved SED are shown in purple dotted (UV, < 3500 Å) and green dash-dotted lines (optical, 4000–6500 Å), respectively. The stacked SED of LRDs in JADES (Pérez-González et al. 2024) and COSMOS-Web surveys (Akins et al. 2024) are shown in grey thick curves and squares, respectively; the upper limits of LRDs in COSMOS-Web survey are shown in grey triangles. All stacked SED are normalized to 0.01 mJy at rest 3000 Å for a direct comparison of the unresolved SED of J2048 and high-z LRDs.

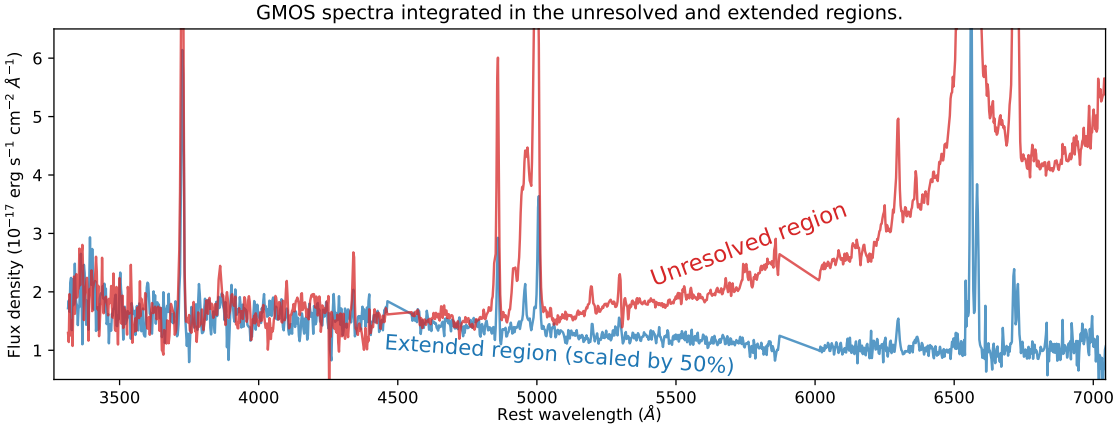

Figure 5. GMOS spectra integrated in the unresolved central region (red) and the extended outskirt region (blue). The extended spectrum is rescaled by 50% to match the continuum flux of the unresolved region at 3500–4500 Å. Only the unresolved region shows a red continuum and a BLR component of Hα line, which are emitted from an obscured AGN. The integration method to create the two spectra are shown in Appendix A with the best-fit models in Figure A3.

5.1. *A LRD analog at low-redshift*

J2048 and the LRDs at $z > 4$ share several common features: (i) a v-shape SED in the UV and optical bands (Figure 4); (ii) a compact red continuum and a broad Hα line component emitted by attenuated AGN (Figure 1 and 3); and (iii) an overmassive location in the M_{BH}-$M_\star$ diagram (Figure 6). These similarities suggest J2048 as a low-z analog of those distant LRDs.

The SED of J2048 is compared with the stacked SED of high-z LRDs in JADES (Pérez-González et al. 2024) and COSMOS-Web surveys (Akins et al. 2024) in Figure 4. For the sake of a direct comparison with SED of high-z LRDs that are typically unresolved, we show the SED from the unresolved region ($r < 2$ kpc) of J2048 in Figure 4 (orange thick line), which is obtained by subtracting the best-fit models of the extended outskirt spectrum[25] from the best-fit SED of the entire galaxy

[25] In order to obtain the SED in the outskirt region, we extend the best-fit stellar continuum model (as shown in Figure A3)

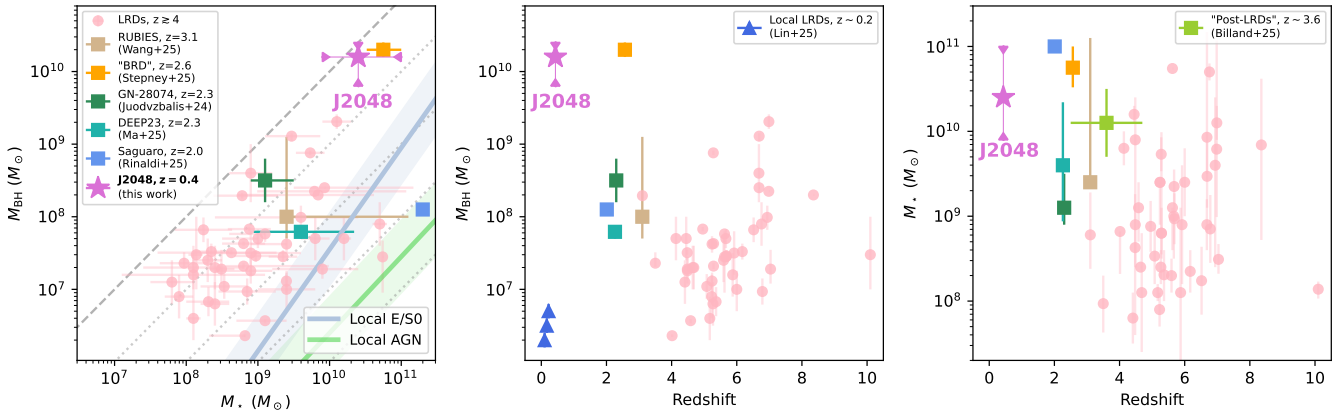

Figure 6. $M_{\rm BH}$ vs. M_* (left), $M_{\rm BH}$ vs. redshift (middle), and M_* vs. redshift (right) diagrams of JWST-discovered LRDs at $z \gtrsim 4$ (pink dots, Goulding et al. 2023; Harikane et al. 2023; Kocevski et al. 2023; Maiolino et al. 2024; Wang et al. 2024; Juodžbalis et al. 2024b; Akins et al. 2025; Kocevski et al. 2025), as well as the lower-z analogs of LRDs at Cosmic Noon (squares, Juodžbalis et al. 2024a; Billand et al. 2025; Ma et al. 2025; Rinaldi et al. 2025; Stepney et al. 2024; Wang et al. 2025) and local universe (triangles, Lin et al. 2025). J2048 is shown as purple stars with the lower- and upper-limits (Section 4.1 and 4.2) denoted in purple triangles. The $M_{\rm BH}$-M_* relations of local AGNs and E/S0-type galaxies are shown with green and blue thick lines, respectively (with ±0.5 dex; Reines & Volonteri 2015). The $M_{\rm BH}/M_* = 1$ locations are shown with grey dashed line; the ratios of 10^{-4}–10^{-1} are shown with grey dotted lines.

(Figure 3). The stacked LRD SED are normalized to 0.01 mJy at rest 3000 Å to compare with the unresolved SED of J2048. The unresolved SED of J2048 is curved due to the Balmer break of a young stellar population formed in ∼ 20 Myr (from continuum fitting) and the red color from the obscured AGN power-law. The unresolved SED of J2048 is very similar to the v-shape SED of the stacked LRD templates in the UV and optical ranges. The approximate power-law indexes in UV (< 3500 Å) and optical range (4000–6500 Å) are estimated to be $\alpha_{\lambda,\rm UV} = -1.5$ and $\alpha_{\lambda,\rm opt} = 1.2$, respectively, which are within the index ranges of high-z LRDs, e.g., $-2.8 < \alpha_{\lambda,\rm UV} < -0.4$ and $0 < \alpha_{\lambda,\rm opt} < 3$ (Figure 3 of Kocevski et al. 2025). Note that the v-shape SED with a red continuum is only detected in the unresolved region ($r < 2$ kpc) of J2048, while the extended region shows a blue continuum emitted by young stars in the optical range (Figure 5 and A3).

The SED of J2048 has an obvious red bump in the NIR range (> 1 μm). We examine the possible contributor of the red bump in Section 3.4, and conclude that a reddened AGN power-law continuum is the only reasonable explanation. The reddened power-law continuum as well as the BLR Hα line indicate an obscured AGN embedded in J2048, which is also considered as a main population in the high-z LRDs (e.g., Maiolino et al. 2024; Greene et al. 2024; Hviding et al. 2025). The SED of J2048 is redder than the stacked LRD SED (Figure 4), which is probably due to the higher extinction of J2048, $A_{V,\rm PL} = 6.3$, compared to the typical values of LRDs, e.g., $A_V = 3$–4 (Kocevski et al. 2025; Li et al. 2025b).

Utilizing the best-fit results of the pure spectral fitting and the simultaneous spectrum+SED fitting, we estimate $M_{\rm BH}$ and $M_\star$ as well as their lower- and upper-limits (Section 4.1 and 4.2), which are shown in Figure 6. The results of the JWST-discovered LRDs at $z \gtrsim 4$ (e.g., Goulding et al. 2023; Harikane et al. 2023; Kocevski et al. 2023; Maiolino et al. 2024; Wang et al. 2024; Juodžbalis et al. 2024b; Akins et al. 2025; Kocevski et al. 2025), as well as the lower-z analogs of LRDs at Cosmic Noon (squares, Juodžbalis et al. 2024a; Billand et al. 2025; Ma et al. 2025; Rinaldi et al. 2025; Stepney et al. 2024; Wang et al. 2025) and local universe (triangles, Lin et al. 2025) are also shown in Figure 6. Despite the large uncertainties in estimation of host stellar mass[26], there is an increasing trend of M_* from LRDs at $z > 4$ (10^8–10^{10} $M_\odot$) to the analogs at Cosmic Noon (10^9–10^{11} $M_\odot$), and J2048 locates at this increasing path towards lower redshift as shown in Figure 6 (right panel). On the other hand, similar to many of the distant LRDs, J2048 also possesses an overmassive SMBH even if we adopt our

to UV and NIR ranges. Since the AGN power-law continuum and torus components emit only in the nuclear region, they are not considered in the subtracting of outskirt SED.

[26] The typical method to estimate M_* with SED fitting can be affected by the choice of SED types, e.g., galaxy-only SED or AGN-host composite SED (e.g. Wang et al. 2024, 2025; Billand et al. 2025). The derived M_* can also be underestimated due to the lack of the faint old stellar population, especially for the LRD analogs at lower redshifts (as discussed in Section 4.2). For M_* estimated based on dynamical mass, the uncertainties can originate from the unconstrained size (e.g., Ma et al. 2025) and the complicated dynamical structure (e.g., Banerji et al. 2021; Stepney et al. 2024).

most conservative estimation of $M_{\rm BH}$ or M_* (Figure 6, left panel). We discuss the overmassive SMBH in details in Section 5.3.

Finally we note the main difference of J2048's spectral features compared to those of high-z LRDs, i.e., no obvious absorption feature on AGN BLR lines in J2048. The absorption line can be associated to the dense gas environments and super-Eddington accretion bursts in high-z LRDs (e.g., Inayoshi 2025). However, the non-detection of such absorption lines in J2048's spectrum does not imply the actual absence of those features, since in the observation only Hα show BLR line while the Hα absorption line could be merged by the complicated outflow profiles of Hα-[NII] complex. Future NIR observations of Paschen lines are required to address if such dense gas absorption exist in J2048.

5.2. *Implications on high-redshift LRDs from observation of J2048*

Thanks to its brightness and low redshift, J2048 serves as a unique laboratory to witness the properties in distant LRDs. One of the major mysteries on LRDs is the reason of the v-shape SED, or in other word, the origin of the blue excess. Either a star-forming galaxy or scattered AGN light is considered as possible explanations of the blue excess. The host star-forming origin is preferred to explain the LRDs with extended features in JWST's imaging observations (e.g., Rinaldi et al. 2024; Billand et al. 2025; Chen et al. 2025a; Zhuang et al. 2025); however, due to the distance of the high-z LRDs, such extended features are usually very faint. The GMOS observation of J2048 clearly exhibit that the extended, blue continuum is emitted by young stars with a SFR of 400 $M_\odot\,{\rm yr}^{-1}$ in the recent $\sim$ 20 Myr. This is the first time that a starburst host galaxy in a LRD-like object is spatially resolved with spectroscopic confirmation. The extended, bright starburst emission also matches the prediction of Billand et al. (2025), i.e., the outskirt component could become more apparent as redshift decrease due to the formation of host galaxies.

Most LRDs at $z > 4$ show weak or non-detections of rest MIR emissions, which implying the lack of dusty tori ($T \simeq$ 300–1500 K) in the vicinity of the SMBHs (e.g., Leung et al. 2024; Pérez-González et al. 2024; Williams et al. 2024; Akins et al. 2024; Setton et al. 2025). A torus is also absent in the "Big Red Dot" at $z \sim 2.5$ (Stepney et al. 2024). A possible explanation is that the AGN is reddened by dust out of the nuclear torus scale (10–30 pc; e.g., Nenkova et al. 2008; Hönig 2019; Nikutta et al. 2021; Li et al. 2025b; Chen et al. 2025b). The AGN torus component is detected in J2048. However, if we redshift the SED of J2048 to $z > 4$ and scale it to the flux level of LRDs at rest 3000 Å, the torus component of J2048 is also below the detection limits of the current LRD surveys at rest MIR bands (e.g., Akins et al. 2024), e.g., Herschel/PACS at 70 and 160 μm ($\sim 10\,\mu$m in rest frame), as shown in Figure 4. As discussed in Section 4.1, the torus-to-bolometric luminosity ratio of J2048, $\sim$ 0.03, is 0.4 dex lower than that of typical normal AGNs (e.g., Ichikawa et al. 2019). The lower ratio suggest that the torus in LRD-like objects could be thinner than that in typical AGNs, i.e., a smaller covering factor, which reduces the absorbed and reemitted energy by torus and results in its faintness. The slim and faint torus scenario can be incorporated into the one with extended absorber to explain the weak MIR features of LRDs.

It is suggested that a powerful outflow can have an important role in the evolution of LRDs, e.g., expelling gas from the inner AGN region, enlarge the galaxy size, enhance or suppress star formation (e.g. Billand et al. 2025; Wang et al. 2025). Outflow features have been seen in a small number of LRDs with JWST/NIRSpec in both of emission lines (e.g., [OIII], Cooper et al. 2025; D'Eugenio et al. 2025) and absorptions (e.g., He I, Juodžbalis et al. 2024a; Wang et al. 2025). Such outflows have also been detected in lower-z LRD analogs with unresolved observations (e.g. Stepney et al. 2024; Lin et al. 2025). J2048 has the first spatially-resolved outflow detection and the most powerful outflow among LRD-like objects. Since the extinction in the AGN central region is high ($A_V \sim 6$) of J2048 and only Hα has the BLR line, the ionized outflow is clearly detected in the [OIII] line profile without contamination of Hβ BLR line. It is fast (-2070 km s^{-1}) and extended to 1 kpc scale, showing high mass-loss rate (160 $M_\odot\,{\rm yr}^{-1}$) and kinetic power ($10^{44.3}$ erg s^{-1}). The finding indicates that such powerful outflow could also occur in high-z LRDs and significantly affect the evolution and environment of those distant galaxies.

The extinction of AGN in J2048, $A_V = 6.3$, is higher than the typical values of LRDs, e.g., $A_V = 3$–4 (Kocevski et al. 2025; Li et al. 2025b). The finding could suggest that LRDs with higher obscuration, or even a buried AGN (i.e., a type-2 SED), may also exist in high-z universe; and there could be a dynamical change of obscuration level driven by AGN feedback via strong radiation or powerful outflows. Those obscured/buried AGN population has not been found yet due to their faintness and the selection upper limit of JWST observations at redshift up to 10. It is implicated that the actual AGN population related to the JWST-discovered distant LRDs could possess even a higher number density than the values based on the current LRDs surveys.

5.3. *An extremely overmassive SMBH*

J2048 has an extremely overmassive SMBH. If we adopt the fiducial estimation, $M_{\rm BH} = 10^{10.2}\ M_\odot$ and $M_* = 10^{10.4}\ M_\odot$ (Section 4.1 and 4.2), the $M_{\rm BH}/M_*$ ratio is derived to be $\simeq 0.6$, which is approximately two orders of magnitude higher than the ratio of local E/S0-type galaxies (Reines & Volonteri 2015) with a similar M_* (Figure 6, left panel). Even if we adopt our most conservative estimation, e.g., the upper limit of M_*, 10^{11}

$M_\odot$(or the lower limit of $M_{\rm BH}$, $10^{9.8}$ $M_\odot$), we still get $M_{\rm BH}/M_* \simeq 0.2$.

Overmassive central BHs (e.g., $M_{\rm BH}/M_* > 0.1$) are found in a large fraction of the LRDs at $z > 4$ (e.g., Inayoshi & Ichikawa 2024; Maiolino et al. 2024; Kocevski et al. 2025). The origin of the overmassive BHs are still debated, possible explanations are underestimation of M_* in SED fitting due to different choices of SED types (e.g., Maiolino et al. 2024; Wang et al. 2024), selection bias of LRD surveys favoring luminous and massive BHs (e.g., Li et al. 2025a), the lag of star formation and less developed stellar bulge at these early epochs (e.g. Maiolino et al. 2024; Juodžbalis et al. 2024b), or the super-Eddington accretion bursts (e.g. Inayoshi & Ichikawa 2024; Juodžbalis et al. 2024b). Such overmassive SMBHs are also discovered in two LRD analogs at cosmic noon, ULASJ2315+0143 (Stepney et al. 2024) and JADES GN-28074 (Juodžbalis et al. 2024a). Overmassive SMBHs are very rare in local universe (e.g., NGC 1277, van den Bosch et al. 2012). J2048 would possess one of the highest $M_{\rm BH}/M_*$ ratio at low redshifts.

In the case of J2048, the possibility of an underestimated M_* can be discarded because J2048 has an overmassive SMBH even if we adopt our most conservative M_* estimation. Galaxy mergers are usually considered to enhance the accretion of central SMBHs (e.g. Hopkins et al. 2008; Sturm et al. 2011; Veilleux et al. 2013; Toba et al. 2022; Yutani et al. 2022). However, the overmassive SMBH of J2048 is unlikely the direct production of the recent merger in past ~ 20 Myr (from stellar continuum fitting). Even if we consider J2048 experienced 10 cycles of such merger events, the mean accretion rate required to construct $M_{\rm BH}$ of $\sim 10^{10}$ $M_\odot$ is still impossibly high (e.g., $\sim$10–100 $M_\odot\,{\rm yr}^{-1}$). Therefore the overmassive SMBH could already be in place before the recent merger event(s). A possible scenario is that, J2048 was a successor of the most massive LRDs at $z > 4$, e.g., CEERS 7902 ($M_{\rm BH} = 10^{9.3}$, $M_\odot$ Kocevski et al. 2025), which already built the bulk of the $M_{\rm BH}$ at early epochs (e.g., via super-Eddington accretion bursts), and then experienced several merger events during Cosmic Noon to possess the observed $M_{\rm BH}$. Meanwhile, unlike most LRDs that left from the overmassive-BH phase as the development of the host stellar components (e.g. Maiolino et al. 2024; Billand et al. 2025), the stellar build-up of J2048 was suppressed due to some reasons (e.g., powerful outflow feedback, or stripping-out of stellar envelope during past mergers), and as a result, the overmassive-BH is retained till the observed epoch.

J2048 is currently in a growing period of both of the SMBH and the host galaxy suggested by the AGN Eddington ratio of 0.14 and the SFR of 400 $M_\odot\,{\rm yr}^{-1}$ (optical/IR-based). However, this active growing phase is likely to be terminated soon since a powerful outflows have been launched (Section 4.4), although currently there is no significant evidence of the occurrence of such strong negative feedback[27] (e.g. Chen et al. 2025c). Furthermore, the current $M_{\rm BH}$ is already comparable to those of the most massive SMBHs in local universe (e.g., Kormendy & Ho 2013; Reines & Volonteri 2015), and it is not probable that J2048 will experience any further significant SMBH growth. Moreover, the host build-up in J2048 is also constrained, which prevent it to migrate into the local $M_{\rm BH}$-M_* relation. A local elliptical galaxy with $M_{\rm BH}$ of $\sim 10^{10}$ $M_\odot$ has a M_* of $\sim 10^{12}$ $M_\odot$. If J2048 could grow up to $M_* = 10^{12}$ $M_\odot$ via star formation in the remaining cosmic time (~ 4.6 Gyr at $z = 0.433$), an average SFR of ~ 200 $M_\odot\,{\rm yr}^{-1}$ over Gyrs is required, which is impossibly high. On the other hand, there is also no potential mass budget for future merger assembling. The Illustris TNG100 simulation suggests a maximum separation of ~ 200 kpc ($\sim 35''$ at $z = 0.433$) for galaxy merger occurring in 4 Gyr (Chamberlain et al. 2024). However, there is no non-stellar objects within $35''$ from J2048 that reaches 1% of the flux of J2048 (19.05 mag in i-band). To summarize, the evolutionary destination of J2048 could be a moderately enlarged stellar bulge with a retained overmassive SMBH.

ACKNOWLEDGMENTS

We kindly appreciate Zhengrong Li for providing the stacked SED of JWST-discovered LRDs. This work is supported by the Japan Society for the Promotion of Science (JSPS) KAKENHI Grant Number 25K17447 (X.C.), 25K01043 (K.I.), 24K00670 (M.A.), 24K22894 (M.O.), and 23H00131 (A.K.I.). K.I. acknowledges support from JST FOREST Program Grant Number JPMJFR2466 and from Inamori Research Grants. M.A. was supported by NAOJ ALMA Scientific Research Grant Code 2023-24A. The observations were carried out within the framework of Subaru-Gemini time exchange program which is operated by the National Astronomical Observatory of Japan. We are honored and grateful for the opportunity of observing the Universe from Maunakea, which has the cultural, historical and natural significance in Hawaii. Data analysis was carried out on the Multi-wavelength Data Analysis System operated by the Astronomy Data Center (ADC), National Astronomical Observatory of Japan.

Facilities: Gemini-N/GMOS, SDSS, 2MASS, WISE, Spitzer

Software: Astropy (Astropy Collaboration et al. 2022), Gemini IRAF (Gemini Observatory & AURA

[27] The instantaneous SFR estimated from narrow Hα or [OII] lines is 20%–40% of the average SFR in the past 10–20 Myr (estimated from optical stellar continuum or far-IR dust emission; see Section 4.2 and 4.3). However, the decreasing trend of SFR is not as significant as those reported in a galaxy with an inaction negative feedback, where SFR decreased over one order of magnitude in past several Myr (Chen et al. 2025c).

2016), Matplotlib (Hunter 2007), PyNeb (Luridiana et al. 2015), `S3Fit`(Chen 2025)

APPENDIX

A. GMOS INTEGRATED SPECTRA IN THE CENTRAL AND OUTSKIRT REGIONS

Figure A3 shows the GMOS integrated spectra in the central and outskirt regions. The central spectrum is created using the average spectra of the central pixels and scaled with the PSF model. The outskirt spectrum is integrated with the GMOS data cube after subtracting the PSF-scaled spectra in the central region. Here we employ the PSF model as the average of the normalized intensity maps of AGN power-law and BLR Hα line, which are obtained with the per-pixel spectral fitting. The PSF can be fit with a Gaussian profile with FWHM of 0.65″ (3.70 kpc) as shown in Figure 1 (right panel).

Since the emission from AGN power-law continuum is highly obscured, the central spectrum at rest $\lambda < 6000$ Å is dominated by stellar continuum emitted by young stars. In the outskirt region where the AGN core components are not detected, the full spectrum in dominated by stellar light. Please refer to Section 4.2 for detailed discussions.

REFERENCES

Akaike, H. 1974, IEEE Transactions on Automatic Control, 19, 716, doi: 10.1109/TAC.1974.1100705

Akins, H. B., Casey, C. M., Lambrides, E., et al. 2024, arXiv e-prints, arXiv:2406.10341, doi: 10.48550/arXiv.2406.10341

Akins, H. B., Casey, C. M., Berg, D. A., et al. 2025, ApJL, 980, L29, doi: 10.3847/2041-8213/adab76

Akiyama, M., He, W., Ikeda, H., et al. 2018, PASJ, 70, S34, doi: 10.1093/pasj/psx091

Ananna, T. T., Bogdán, Á., Kovács, O. E., Natarajan, P., & Hickox, R. C. 2024, ApJL, 969, L18, doi: 10.3847/2041-8213/ad5669

Astropy Collaboration, Price-Whelan, A. M., Lim, P. L., et al. 2022, ApJ, 935, 167, doi: 10.3847/1538-4357/ac7c74

Baldwin, J. A., Phillips, M. M., & Terlevich, R. 1981, PASP, 93, 5, doi: 10.1086/130766

Banerji, M., Jones, G. C., Carniani, S., DeGraf, C., & Wagg, J. 2021, MNRAS, 503, 5583, doi: 10.1093/mnras/stab852

Barro, G., Pérez-González, P. G., Kocevski, D. D., et al. 2024, ApJ, 963, 128, doi: 10.3847/1538-4357/ad167e

Bevington, P. R., & Robinson, D. K. 2003, Data reduction and error analysis for the physical sciences

Billand, J.-B., Elbaz, D., Gentile, F., et al. 2025, arXiv e-prints, arXiv:2507.04011, doi: 10.48550/arXiv.2507.04011

Burnham, K. P., & Anderson, D. R. 2002, Model Selection and Multimodel Inference: A Practical Information-Theoretic Approach, 2nd edn. (New York: Springer)

Calzetti, D. 1997, in American Institute of Physics Conference Series, Vol. 408, The ultraviolet universe at low and High redshift, ed. W. H. Waller, 403–412, doi: 10.1063/1.53764

Calzetti, D. 2013, in Secular Evolution of Galaxies, ed. J. Falcón-Barroso & J. H. Knapen, 419, doi: 10.48550/arXiv.1208.2997

Calzetti, D., Armus, L., Bohlin, R. C., et al. 2000, ApJ, 533, 682, doi: 10.1086/308692

Casey, C. M., Akins, H. B., Finkelstein, S. L., et al. 2025, arXiv e-prints, arXiv:2505.18873, doi: 10.48550/arXiv.2505.18873

Chamberlain, K., Patel, E., Besla, G., Torrey, P., & Rodriguez-Gomez, V. 2024, ApJ, 975, 104, doi: 10.3847/1538-4357/ad7bad

Charlot, S., & Fall, S. M. 2000, ApJ, 539, 718, doi: 10.1086/309250

Chen, C.-H., Ho, L. C., Li, R., & Zhuang, M.-Y. 2025a, ApJ, 983, 60, doi: 10.3847/1538-4357/ada93a

Chen, K., Li, Z., Inayoshi, K., & Ho, L. C. 2025b, arXiv e-prints, arXiv:2505.22600, doi: 10.48550/arXiv.2505.22600

Chen, X. 2025, S3Fit: Simultaneous Spectrum and photometric-SED Fitting code for galaxy observations, Astrophysics Source Code Library, record ascl:2503.024

Chen, X., Akiyama, M., Ichikawa, K., et al. 2020, ApJ, 900, 51, doi: 10.3847/1538-4357/aba599

—. 2025c, ApJ, 979, 32, doi: 10.3847/1538-4357/ad93ab

Cooper, R. A., Caputi, K. I., Iani, E., et al. 2025, arXiv e-prints, arXiv:2502.18310, doi: 10.48550/arXiv.2502.18310

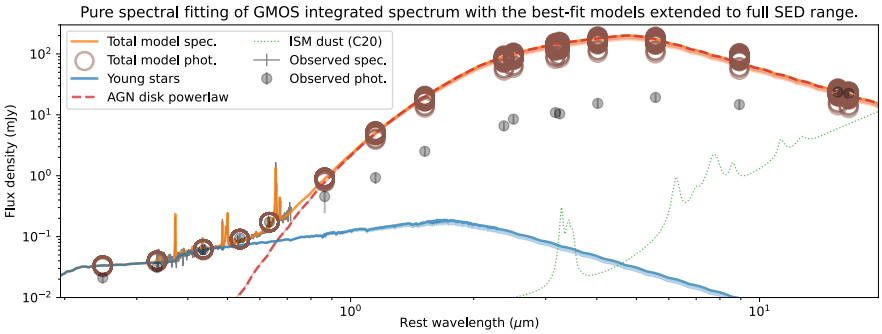

Figure A1. Best-fit models of the pure spectral fitting for the GMOS integrated spectrum of the entire galaxy. The models are extended to the wavelength range covered by the photometric SED. The result suggests that the red power-law continuum is not well constrained with pure spectral fitting due to the limited wavelength coverage. See Section 3.3 for detailed discussion.

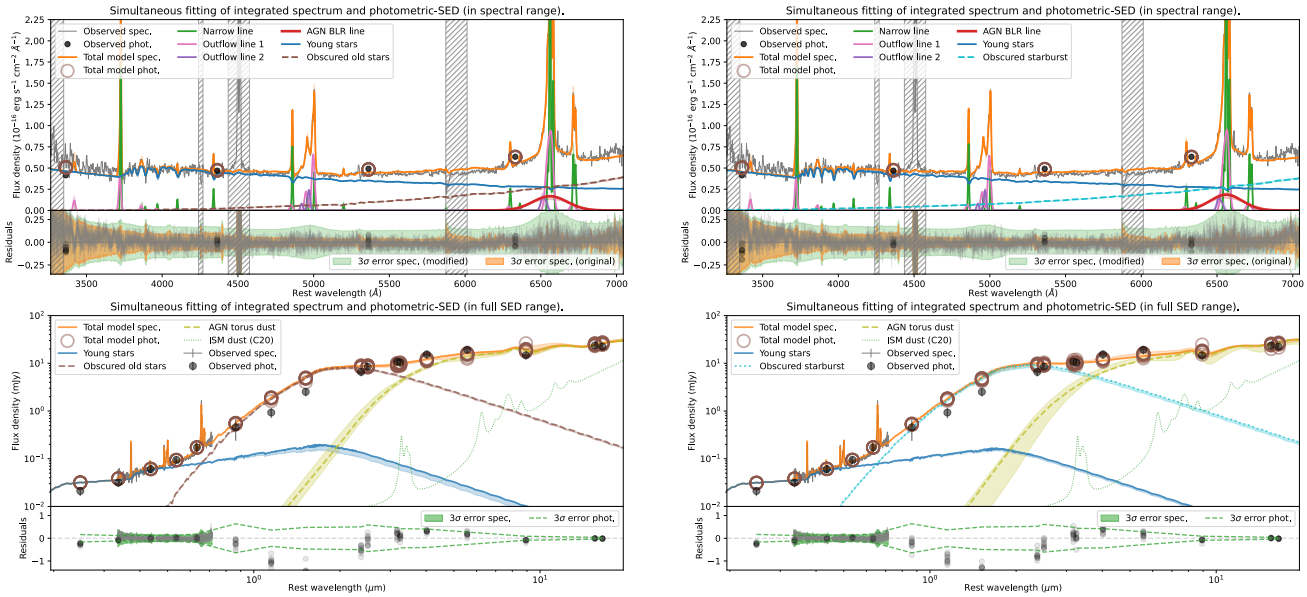

Figure A2. Best-fit results of the simultaneous spectrum+SED fitting in the test cases using (1) an obscured old stellar population (brown dashed curve in the left panels) or (2) a hidden starburst component (cyan dotted curves in the right panels) to reproduce the observed red bump in NIR SED. See Section 3.4 for detailed discussion.

D'Eugenio, F., Juodžbalis, I., Ji, X., et al. 2025, arXiv e-prints, arXiv:2506.14870, doi: 10.48550/arXiv.2506.14870

Duras, F., Bongiorno, A., Ricci, F., et al. 2020, A&A, 636, A73, doi: 10.1051/0004-6361/201936817

Euclid Collaboration, Bisigello, L., Rodighiero, G., et al. 2025, arXiv e-prints, arXiv:2503.15323, doi: 10.48550/arXiv.2503.15323

Feltre, A., Hatziminaoglou, E., Fritz, J., & Franceschini, A. 2012, MNRAS, 426, 120, doi: 10.1111/j.1365-2966.2012.21695.x

Fiore, F., Feruglio, C., Shankar, F., et al. 2017, A&A, 601, A143, doi: 10.1051/0004-6361/201629478

Francis, P. J., Hewett, P. C., Foltz, C. B., et al. 1991, ApJ, 373, 465, doi: 10.1086/170066

Furtak, L. J., Zitrin, A., Plat, A., et al. 2023, ApJ, 952, 142, doi: 10.3847/1538-4357/acdc9d

Gemini Observatory, & AURA. 2016, Gemini IRAF: Data reduction software for the Gemini telescopes, Astrophysics Source Code Library, record ascl:1608.006

Goulding, A. D., Greene, J. E., Setton, D. J., et al. 2023, ApJL, 955, L24, doi: 10.3847/2041-8213/acf7c5

Greene, J. E., & Ho, L. C. 2005, ApJ, 630, 122, doi: 10.1086/431897

Greene, J. E., Labbe, I., Goulding, A. D., et al. 2024, ApJ, 964, 39, doi: 10.3847/1538-4357/ad1e5f

Harikane, Y., Zhang, Y., Nakajima, K., et al. 2023, ApJ, 959, 39, doi: 10.3847/1538-4357/ad029e

He, W., Akiyama, M., Enoki, M., et al. 2024, ApJ, 962, 152, doi: 10.3847/1538-4357/ad1518

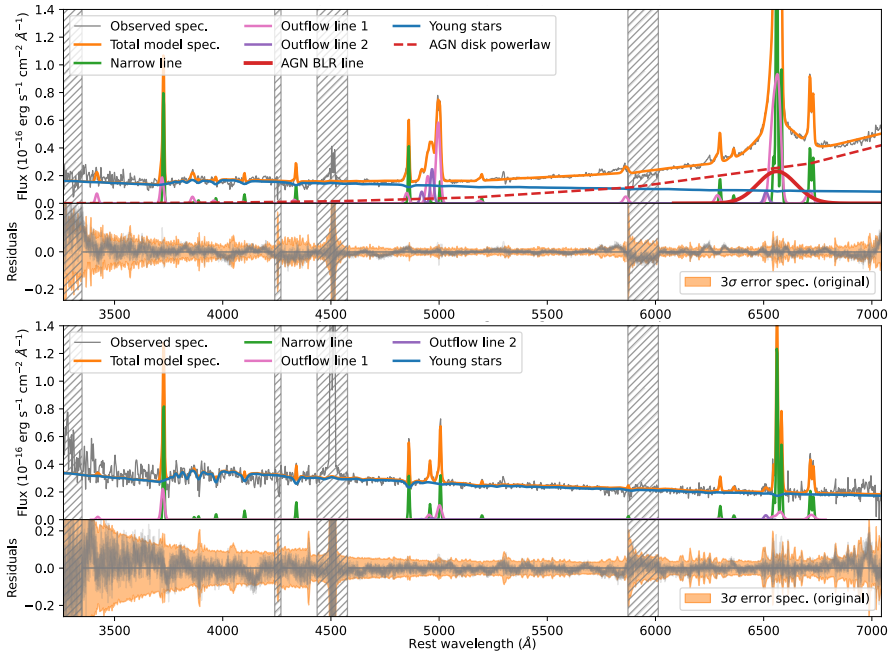

Figure A3. GMOS spectra integrated in the central (PSF-scaled, top and upper-middle) and outskirt regions (lower-middle and bottom). The best-fit models from the pure spectral fitting are shown with the same legends used in Figure 2.

Hönig, S. F. 2019, ApJ, 884, 171, doi: 10.3847/1538-4357/ab4591

Hopkins, P. F., Hernquist, L., Cox, T. J., & Kereš, D. 2008, ApJS, 175, 356, doi: 10.1086/524362

Hummer, D. G., & Storey, P. J. 1987, MNRAS, 224, 801, doi: 10.1093/mnras/224.3.801

Hunter, J. D. 2007, Computing in Science & Engineering, 9, 90, doi: 10.1109/MCSE.2007.55

Hviding, R. E., de Graaff, A., Miller, T. B., et al. 2025, arXiv e-prints, arXiv:2506.05459, doi: 10.48550/arXiv.2506.05459

Ichikawa, K., Ricci, C., Ueda, Y., et al. 2019, ApJ, 870, 31, doi: 10.3847/1538-4357/aaef8f

Inayoshi, K. 2025, arXiv e-prints, arXiv:2503.05537, doi: 10.48550/arXiv.2503.05537

Inayoshi, K., & Ichikawa, K. 2024, ApJL, 973, L49, doi: 10.3847/2041-8213/ad74e2

Inayoshi, K., Kimura, S. S., & Noda, H. 2024, arXiv e-prints, arXiv:2412.03653, doi: 10.48550/arXiv.2412.03653

Jun, H. D., Im, M., Lee, H. M., et al. 2015, ApJ, 806, 109, doi: 10.1088/0004-637X/806/1/109

Juodžbalis, I., Ji, X., Maiolino, R., et al. 2024a, MNRAS, 535, 853, doi: 10.1093/mnras/stae2367

Juodžbalis, I., Maiolino, R., Baker, W. M., et al. 2024b, Nature, 636, 594, doi: 10.1038/s41586-024-08210-5

Kass, R. E., & Raftery, A. E. 1995, Journal of the American Statistical Association, 90, 773, doi: 10.1080/01621459.1995.10476572

Kauffmann, G., Heckman, T. M., Tremonti, C., et al. 2003, MNRAS, 346, 1055, doi: 10.1111/j.1365-2966.2003.07154.x

Kennicutt, Robert C., J., Hao, C.-N., Calzetti, D., et al. 2009, ApJ, 703, 1672, doi: 10.1088/0004-637X/703/2/1672

Kewley, L. J., Dopita, M. A., Sutherland, R. S., Heisler, C. A., & Trevena, J. 2001, ApJ, 556, 121, doi: 10.1086/321545

Kocevski, D. D., Onoue, M., Inayoshi, K., et al. 2023, ApJL, 954, L4, doi: 10.3847/2041-8213/ace5a0

Kocevski, D. D., Finkelstein, S. L., Barro, G., et al. 2025, ApJ, 986, 126, doi: 10.3847/1538-4357/adbc7d

Kokorev, V., Fujimoto, S., Labbe, I., et al. 2023, ApJL, 957, L7, doi: 10.3847/2041-8213/ad037a

Kokorev, V., Caputi, K. I., Greene, J. E., et al. 2024, ApJ, 968, 38, doi: 10.3847/1538-4357/ad4265

Kormendy, J., & Ho, L. C. 2013, ARA&A, 51, 511, doi: 10.1146/annurev-astro-082708-101811

Kroupa, P. 2001, MNRAS, 322, 231, doi: 10.1046/j.1365-8711.2001.04022.x

Kulkarni, G., Worseck, G., & Hennawi, J. F. 2019, MNRAS, 488, 1035, doi: 10.1093/mnras/stz1493

Leung, G. C. K., Finkelstein, S. L., Pérez-González, P. G., et al. 2024, arXiv e-prints, arXiv:2411.12005, doi: 10.48550/arXiv.2411.12005

Li, J., Silverman, J. D., Shen, Y., et al. 2025a, ApJ, 981, 19, doi: 10.3847/1538-4357/ada603

Li, Z., Inayoshi, K., Chen, K., Ichikawa, K., & Ho, L. C. 2025b, ApJ, 980, 36, doi: 10.3847/1538-4357/ada5fb

Liddle, A. R. 2007, Monthly Notices of the Royal Astronomical Society, 377, L74, doi: 10.1111/j.1745-3933.2007.00306.x

Lin, X., Fan, X., Cai, Z., et al. 2025, arXiv e-prints, arXiv:2507.10659, doi: 10.48550/arXiv.2507.10659

Luridiana, V., Morisset, C., & Shaw, R. A. 2015, A&A, 573, A42, doi: 10.1051/0004-6361/201323152

Ma, Y., Greene, J. E., Setton, D. J., et al. 2025, arXiv e-prints, arXiv:2504.08032, doi: 10.48550/arXiv.2504.08032

Maiolino, R., Scholtz, J., Curtis-Lake, E., et al. 2024, A&A, 691, A145, doi: 10.1051/0004-6361/202347640

Matsuoka, Y., Strauss, M. A., Kashikawa, N., et al. 2018, ApJ, 869, 150, doi: 10.3847/1538-4357/aaee7a

Matsuoka, Y., Onoue, M., Iwasawa, K., et al. 2023, ApJL, 949, L42, doi: 10.3847/2041-8213/acd69f

Matthee, J., Naidu, R. P., Brammer, G., et al. 2024, ApJ, 963, 129, doi: 10.3847/1538-4357/ad2345

Millán-Irigoyen, I., Mollá, M., Cerviño, M., et al. 2021, MNRAS, 506, 4781, doi: 10.1093/mnras/stab1969

Nenkova, M., Sirocky, M. M., Ivezić, Ž., & Elitzur, M. 2008, ApJ, 685, 147, doi: 10.1086/590482

Niida, M., Nagao, T., Ikeda, H., et al. 2020, ApJ, 904, 89, doi: 10.3847/1538-4357/abbe11

Nikutta, R., Lopez-Rodriguez, E., Ichikawa, K., et al. 2021, ApJ, 919, 136, doi: 10.3847/1538-4357/ac06a6

Noboriguchi, A., Inoue, A. K., Nagao, T., Toba, Y., & Misawa, T. 2023, ApJL, 959, L14, doi: 10.3847/2041-8213/ad0e00

Pérez-González, P. G., Barro, G., Rieke, G. H., et al. 2024, ApJ, 968, 4, doi: 10.3847/1538-4357/ad38bb

Pérez-Torres, M., Mattila, S., Alonso-Herrero, A., Aalto, S., & Efstathiou, A. 2021, A&A Rv, 29, 2, doi: 10.1007/s00159-020-00128-x

Planck Collaboration, Aghanim, N., Akrami, Y., et al. 2020, A&A, 641, A6, doi: 10.1051/0004-6361/201833910

Reines, A. E., & Volonteri, M. 2015, ApJ, 813, 82, doi: 10.1088/0004-637X/813/2/82

Rinaldi, P., Bonaventura, N., Rieke, G. H., et al. 2024, arXiv e-prints, arXiv:2411.14383, doi: 10.48550/arXiv.2411.14383

Rinaldi, P., Rieke, G. H., Wu, Z., et al. 2025, arXiv e-prints, arXiv:2507.17738, doi: 10.48550/arXiv.2507.17738

Schartmann, M., Meisenheimer, K., Camenzind, M., Wolf, S., & Henning, T. 2005, A&A, 437, 861, doi: 10.1051/0004-6361:20042363

Schwarz, G. 1978, Annals of Statistics, 6, 461, doi: 10.1214/aos/1176344136

Selsing, J., Fynbo, J. P. U., Christensen, L., & Krogager, J. K. 2016, A&A, 585, A87, doi: 10.1051/0004-6361/201527096

Setton, D. J., Greene, J. E., de Graaff, A., et al. 2024, arXiv e-prints, arXiv:2411.03424, doi: 10.48550/arXiv.2411.03424

Setton, D. J., Greene, J. E., Spilker, J. S., et al. 2025, arXiv e-prints, arXiv:2503.02059, doi: 10.48550/arXiv.2503.02059

Shen, Y., & Liu, X. 2012, ApJ, 753, 125, doi: 10.1088/0004-637X/753/2/125

Stalevski, M., Ricci, C., Ueda, Y., et al. 2016, MNRAS, 458, 2288, doi: 10.1093/mnras/stw444

Stepney, M., Banerji, M., Tang, S., et al. 2024, MNRAS, 533, 2948, doi: 10.1093/mnras/stae1970

Storey, P. J., & Zeippen, C. J. 2000, MNRAS, 312, 813, doi: 10.1046/j.1365-8711.2000.03184.x

Sturm, E., González-Alfonso, E., Veilleux, S., et al. 2011, ApJL, 733, L16, doi: 10.1088/2041-8205/733/1/L16

Takeuchi, T. T. 2000, Astrophysics and Space Science, 271, 213, doi: 10.1023/A:1002424903934

Temple, M. J., Hewett, P. C., & Banerji, M. 2021, MNRAS, 508, 737, doi: 10.1093/mnras/stab2586

Toba, Y., Yamada, S., Matsubayashi, K., et al. 2022, PASJ, 74, 1356, doi: 10.1093/pasj/psac073

van den Bosch, R. C. E., Gebhardt, K., Gültekin, K., et al. 2012, Nature, 491, 729, doi: 10.1038/nature11592

Vanden Berk, D. E., Richards, G. T., Bauer, A., et al. 2001, AJ, 122, 549, doi: 10.1086/321167

Veilleux, S., Meléndez, M., Sturm, E., et al. 2013, ApJ, 776, 27, doi: 10.1088/0004-637X/776/1/27

Wall, J. V., & Jenkins, C. R. 2012, Practical Statistics for Astronomers

Wang, B., Leja, J., de Graaff, A., et al. 2024, ApJL, 969, L13, doi: 10.3847/2041-8213/ad55f7

Wang, B., de Graaff, A., Davies, R. L., et al. 2025, ApJ, 984, 121, doi: 10.3847/1538-4357/adc1ca

Williams, C. C., Alberts, S., Ji, Z., et al. 2024, ApJ, 968, 34, doi: 10.3847/1538-4357/ad3f17

Yue, M., Eilers, A.-C., Ananna, T. T., et al. 2024, ApJL, 974, L26, doi: 10.3847/2041-8213/ad7eba

Yutani, N., Toba, Y., Baba, S., & Wada, K. 2022, ApJ, 936, 118, doi: 10.3847/1538-4357/ac87a2

Zhuang, M.-Y., Li, J., Shen, Y., et al. 2025, arXiv e-prints, arXiv:2505.20393, doi: 10.48550/arXiv.2505.20393